Contents

1 Geometry of a Mössbauer measurement

1.1 Moving source

The standard configuration of source, absorber and detector of a Mössbauer experiment is depicted in Fig. 1. The source is mounted on a drive unit and moves $S(v)$ between positions S_{min} and S_{max}, the absorber is at rest between source and detector. As indicated in Fig. 1 the solid angle changes with the position of the source. The variation of the solid angle shall be included in the theoretical description of the experimental data. Prerequisite is a well defined geometry. The detector area has to be large enough not to miss γ-radiation at the edge of the cone of the varying solid angle. In addition the detection efficiency is assumed to be constant over the detector area.

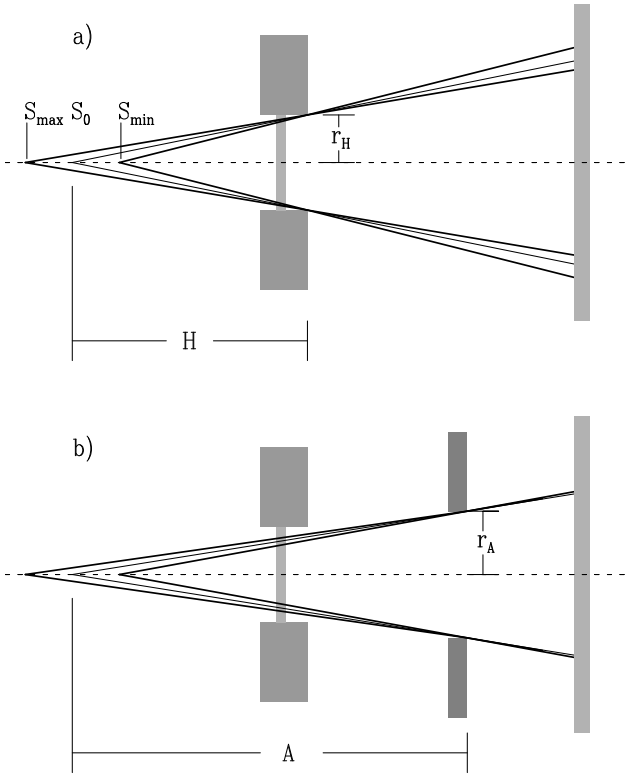

Figure 1: Source is moving between $S_{max} \leq S_0 \leq S_{min}$ and the absorber is fixed at the distance H from position S_0. The solid angle subtended by the detector reaches its maximum at the source position S_{min} and is determined by H plus the displacement of the source and the radius r_H of the absorber holder. In Fig. a) a uniform efficiency almost right up to the edge is presupposed. The aperture (Fig. b)) the solid angle depends on the distance A and radius r_A instead and is decreased to the safe region of the detector area.

The source holder is the aperture diaphragm in (Fig. 1a)). The solid

angle is determined by the actual distance $H + S(v)$ and its shape. In Fig. 1b) an extra aperture diaphragm at a distance A from the $v = 0$ position S_0 of the source in front of the detector determines the solid angle and restricts the γ-radiation to the best (homogeneously) region of the detector.
This geometry is well suitable for an absorber in a cryostat.

1.2 Moving absorber

The moving absorber in most cases is used as an analyzer and the source at rest in a cryostat the object of research. In this case the geometry in Fig. 2a) is the most favorable one since the solid angle is independent on the velocity. This geometry can be always achieved by an aperture diaphragm in front of the detector. The condition of homogeneity of the detector is not any more required. The situation Fig. 2b) should be avoided.

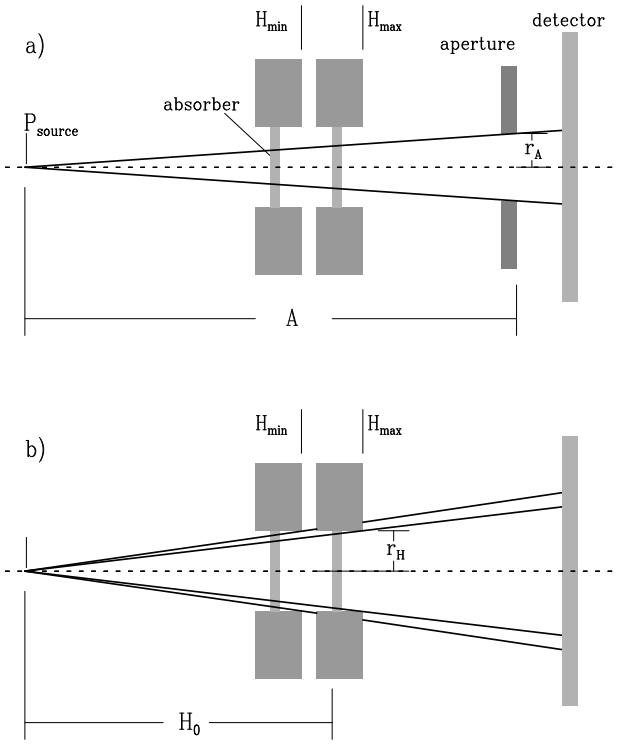

Figure 2: Source at position P_{source} is fixed and the absorber is moving between the distances from the source H_{min} and H_{max}. With the aperture of radius r_A at a distance A from the source (Fig. a)) the solid angle subtended by the detector at a point source depends on A and r_A and not on the position of the absorber. Removing the aperture (Fig. b)) the solid angle becomes larger and depends on the position of the absorber. The figure emphasizes the dependence on the dimensions of the absorber holder, the distance $H_{min} \leq H \leq H_{max}$ and the radius r_H.

2 Baseline

The measurement of the baseline of a Mössbauer spectrum already provides valuable information about the equipment, that is the geometry and dead time effects. In a first step the geometry effect of the moving source both in triangular and sinusoidal mode in the limit of large distances from the detector or aperture in front of the detector shall be considered. The distance law $1/r^2$ for the intensity of radiation at distance r from the isotropically radiating source leads to a type of sinusoidal modulation of the baseline. At large distances the source can be approximated by a point source and the shape of the aperture plays no role. This case is outlined first. Then the corrections for short distances for a point source and afterwards for an extended source are considered. The latter can only be done numerically. Three types of shape of the aperture are discussed, that are the most common circular aperture, the square or rectangular shape and the special case of an elliptical shape oriented at an angle α which were used for a series of single crystal measurements.

2.1 Shape of the baseline

The dependence of the count rate on the position S of the source at channel number k is given by the distance r_k. In case of a sinusoidal motion of the source $S = S_{max}\sin(\omega t)$ with the distance $r(t) = A + S(t)$ to the aperture the largest distance $A + S_{max}$ and lowest count rate is reached at time $t = T/4$. At $t = 3/4T$ the distance is $A - S_{max}$ with the highest count rate. The count rate is proportional to $1/(A + S(k))^2$ which gives some kind of sinusoidal modulation of the baseline as shown in Fig.3. In multi scaling mode the channel number k is proportional to time t such that at the full period time T the counts are collected in the highest channel K. Time t is expressed by channel k according $t = k \cdot T/K$. The velocity $v(t) = dS/dt = S_{max}\omega \cdot \cos(\omega t)$ starts at $t = 0$ with $v_{max} = S_{max}\omega$ and reaches at $t = T/4$ corresponding to channel $k = 512$ zero velocity.
The geometry effect is well characterized by the parameter $geo = S_{max}/A$. If N_0 is the number of counts with the source at rest ($S(k) = 0$) the num-

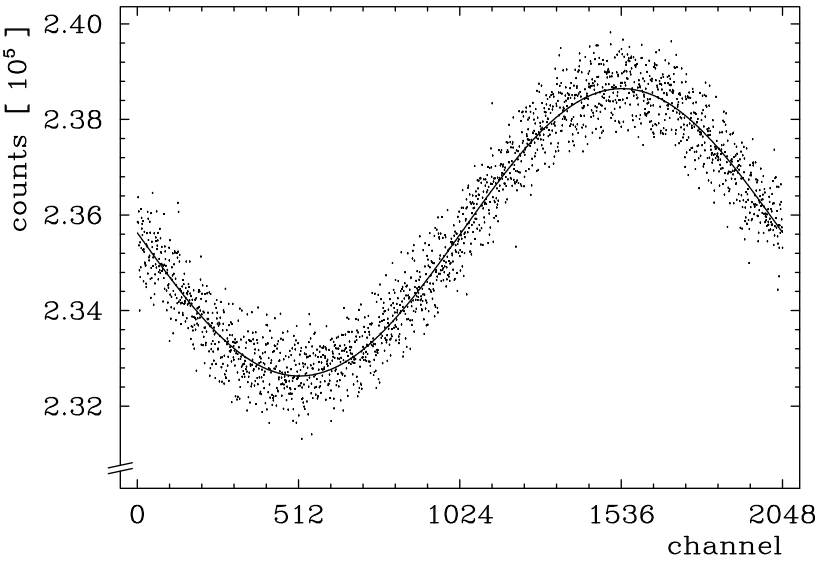

Figure 3: The baseline of $2.4 \cdot 10^5$ counts measured with the sinusoidal mode shows the characteristic geometry effect. The $\chi^2 = 1.030$ value deviates from 1 by less than $1\sigma = \sqrt{2}/\sqrt{K = 2048} = 0.031$.

ber of counts $N(k)$ (Fig.3) is written as:

$$\begin{aligned} N &= N_0 \frac{A^2}{(A + S(k))^2} = \frac{N_0}{(1 + \frac{S(k)}{A})^2} \\ &= \frac{N_0}{(1 + \frac{S_{max}}{A}\frac{S(k)}{S_{max}})^2} \\ &= \frac{N_0}{(1 + geo \cdot \sin(2\pi/K \cdot k))^2} \end{aligned} \tag{1}$$

The argument ωt is replaced by $2\pi/T \cdot (T/K)k$.

For later use the source position S is expressed by the dependence on its velocity v replacing the sin function by $\pm\sqrt{1 - \cos^2}$ and S_{max} replacing ω by $2\pi/T$

$$\begin{aligned} S(v) &= \pm S_{max}\sqrt{1 - \left(\frac{v}{v_{max}}\right)^2} \\ S_{max} &= \frac{v_{max}}{2\pi}T \end{aligned} \tag{2}$$

The same consideration for the triangular mode requires some lengthy evaluation. Starting at $t = 0$ and $v = v_{max}$ the acceleration b in the opposite direction decreases the velocity to zero in a quarter of a period

$T/4$.

$$v(t) = v_{max} + bt$$

Integration of $v(t)$ with the boundary condition $S(t = 0) = 0$ gives

$$S(t) = v_{max}t + \frac{1}{2}bt^2 \tag{3}$$

At $t = T/4$ the velocity is zero, so that from Eq. 3 $v_{max} = -bT/4$, and the source gets the maximum deviation S_{max}. Inserting $t = T/4$ and $b = -4v_{max}/T$ the maximal deviation in the triangular mode is obtained

$$S_{max} = \frac{v_{max}}{8}T \tag{4}$$

The dependency of S on the velocity v is obtained inserting t from Eq. 3 into $S(t)$ and using $v_{max} = -bT/4$ from above.

$$\begin{aligned} S(v) &= v_{max}\frac{v - v_{max}}{b} + \frac{1}{2}b\left(\frac{v - v_{max}}{b}\right)^2 \\ S(v) &= +S_{max}\left(1 - \left(\frac{v}{v_{max}}\right)^2\right) \end{aligned} \tag{5}$$

The second half period starting at $t = T/2$ with $v(t = T/2) = -v_{max}$

$$v(t) = -v_{max} + b(t - \frac{T}{2})$$

yields the same expression for $S(v)$ with the minus sign. Similar to the Eqs.2 for the sinusoidal case the equations for the triangular case are

$$\begin{aligned} S(v) &= \pm S_{max}\left(1 - \left(\frac{v}{v_{max}}\right)^2\right) \\ S_{max} &= \frac{v_{max}}{8}T \end{aligned} \tag{6}$$

Note the differences of the equations. Fig.4 shows the difference of the baselines of the 2 modes with the same parameter $geo = S_{max}/A$. The curve of Fig.3 fitted to experimental points measured with the sinusoidal mode has been recalculated with the triangular mode.

2.2 Solid angle of a point source

The modulation of the baseline as considered above is only an approximation valid for large distances. It is proportional to the ratio of the

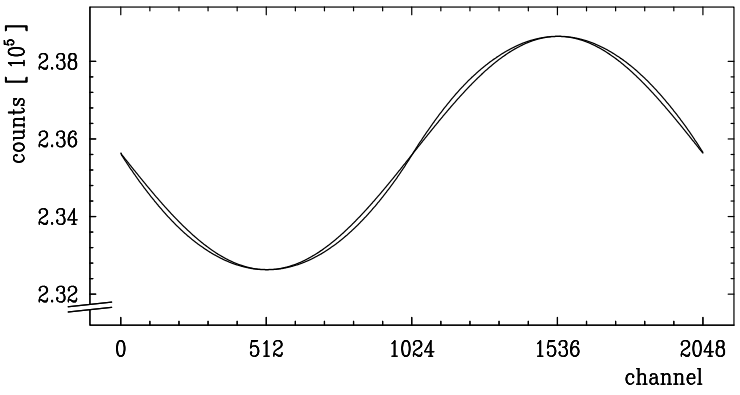

Figure 4: The fitted baseline of of Fig.3 measured with the sinusoidal mode is compared with the curve calculated with the triangular mode. The slope of the curve belonging to the triangular mode turns out to be larger.

solid angles $\Omega(S)/\Omega(S=0)$ subtended at the point source by an aperture and depends also on the shape. In the following the solid angles for apertures of the shape of a circle, a square and an ellipse are discussed.

2.2.1 Solid angle of a circle

The intensity of the radiation from the source S through an aperture proportional to the solid angle Ω determined by the position of the source relative to the aperture. The simplest case is a point source on the axis orthonormal to the aperture as shown in Fig. 5.
The surface of the infinitesimal ring element from r to $r+\delta r$ of the aperture is $2\pi r\delta r$. The ring element resects from the surface of the sphere with radius $R=\sqrt{r^2+A^2}$ the element $2\pi r\delta r\cdot\cos\vartheta$. The solid angle $d\Omega$ of the surface element is given by the sphere of radius 1 such that

$$\begin{aligned} d\Omega &= 2\pi r\delta r\cdot\cos\vartheta/R^2 \quad with \\ tg\vartheta &= r/A \end{aligned}$$

The solid angle is obtained by integration over r. With the identity

$$\begin{aligned} \cos\vartheta(r) &= \cos(\arctan(r/A)) \\ &= \frac{1}{\sqrt{1+(\frac{r}{A})^2}} \end{aligned}$$

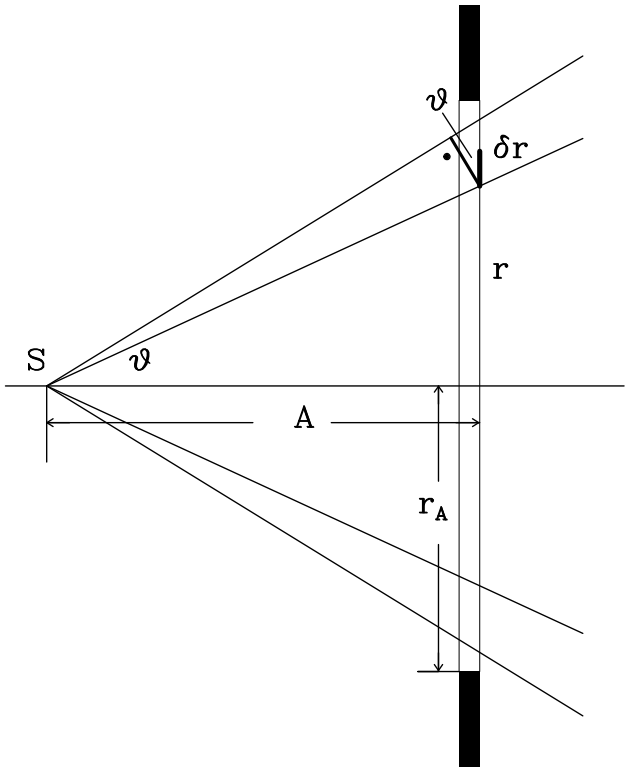

Figure 5: Source at position S, an aperture at a distance A is centered to an optical axis. The solid angle $d\Omega$ belonging to the surface element at r and width δr is equal to the projection of the surface element $2\pi r\delta r \cdot \cos\vartheta$ onto the unit sphere. The point near ϑ marks the angle $\pi/2$.

the integral is written as

$$\begin{aligned}\Omega &= 2\pi \int_0^{r_A} \frac{Ardr}{(r^2+A^2)\sqrt{(r^2+A^2}} \\ &= 2\pi \int_0^{r_A} \frac{1}{2} dx^2 \left(1+x^2\right)^{-\frac{3}{2}} \quad with \quad x = r/A\end{aligned}$$

which is evaluated to be

$$\Omega = 2\pi \left(1 - \frac{1}{\sqrt{1+\left(\frac{r_A}{A}\right)^2}} \right) \tag{7}$$

For the experimental cases with ratios $r_A/A << 1$ the Taylor expansion is sufficient. Denoting the area πr_A^2 by F_A the solid angle becomes

$$\Omega = \frac{F_A}{A^2}\left(1 - \frac{3}{4\pi}\frac{F_A}{A^2} + ...\right) \tag{8}$$

The distance $r(S)$ of the moving source is $A + S$. With $\delta = S/A$ and

$\tau = F_A/A^2$ the ratio

$$\frac{\Omega(S)}{\Omega(0)} = \frac{1}{\delta)^2}\left(1 - \frac{57}{16\pi^2}\tau^2 + \frac{3}{2\pi}\tau\delta + \frac{9}{8\pi^2}\tau^2\delta\right) \tag{9}$$

is well approximated by $1/(1+\delta)^2$. Even for typical apertures of an area $F_A = 1cm^2$ at small distances $A = 25mm$ the product $\tau\delta$ turns out to be very small compared to 1. Taking $v_{max} = 10\,mm/s$ and $1/T = 10Hz$ the ratio $\delta(v = 0) = S_{max}/A$ becomes $5 \cdot 10^{-3}$ which together with $\tau = F_A/A^2 = 0.16$ gives $\delta\tau = 8 \cdot 10^{-4}$ (neglection of τ^2-terms).

2.2.2 Solid angle of a square

There exist also an analytical solution for the solid angle of a rectangular aperture of of length a and width b at a distance A [1]. With the definition of two parameters $\alpha = (a/2)/A$ and$\beta = (b/2)/A)$ the solid angle is given by

$$\Omega(a, b, A) = 4\arccos\sqrt{\frac{1+\alpha^2+\beta^2}{(1+\alpha^2)(1+\beta^2)}} \tag{10}$$

An expansion to the order $(\alpha\beta)^4$ is also accomplished in [1].

$$\Omega(a, b, A) \;=\; 4\alpha\beta - 2\alpha\beta(\alpha^2+\beta^2) + ...$$

The solid angle of the square (a=b) with $F = a^2$ is similar to Eq. 8

$$\Omega = \frac{F}{A^2}\left(1 - \frac{1}{4}\frac{F}{A^2} + ...\right) \tag{11}$$

The comparison with the circular aperture shows that the correction which differs by the ratio $3/\pi$ can be neglected by the same argument.

2.2.3 Solid angle of an ellipse

The crystal orientation technique involves rotation of the crystal on a single-circle goniometer inclined at fixed angle ($\alpha = 45^o$) about an axis fixed in the crystal; the gamma beam then traces out a right (circular) cone in the crystal. The technique has been described analytically by Weil, Buch and Clapp[2] and has been utilized by Spiering and Vogel [3] in their single-crystal Mössbauer study of FeCl2·4H2O and later several times by Bull et al. [4, 5, 6] using the geometry of Fig.6 where the cut of

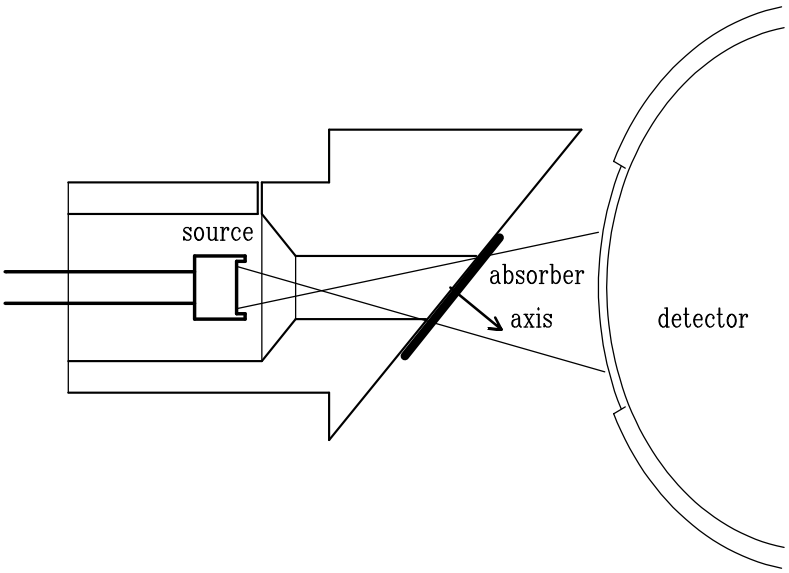

Figure 6: Configuration of source, absorber and detector (proportional counter) for a series of measurements at different γ-directions with respect to the single crystal absorber as used in the work of Bull et al. [4, 5, 6]. The different γ-directions are obtained by rotation around the axis orthonormal to the absorber plate which includes an angle $\alpha = 45^o$ with the optical axis defined by the direction of the velocity vector of the source. The aperture given by the cut at $\alpha \neq 0^o$ of the cylindrical bore hole is an ellipse. the asymmetric radiation cone is depicted for an extended source.

the guide tube for the γ-radiation at an angle $\alpha < 90^o$ gives the aperture an elliptical shape.
There exist analytical formulas to calculate the solid angle subtended at an arbitrarily positioned point source by an elliptically shaped aperture. In the paper of Abbas et al.[7] six cases concerning the positions of the source are considered. The first and plainest case is that of an elliptically shaped aperture with an isotropic radiating central point source at distance z=A. The solid angle is given by:

$$\Omega(0,0,A) = \int_0^{2\pi} \int_0^{\theta(\phi)} \sin\theta d\theta d\phi \tag{12}$$

where the function $\theta(\phi)$ depends on the principal axes a and b.

$$\begin{aligned} \theta(\phi) &= \arctan(r(\phi)/A)) \\ r(\phi) &= \frac{ab}{\sqrt{(a\cdot\sin(\phi))^2 + (b\cdot\cos(\phi))^2}} \end{aligned}$$

The result for the circle of Eq. 8 is readily obtained setting a=b. Introducing the eccentricity $\epsilon = \sqrt{a^2 - b^2}/a$ and the area $F = \pi ab$ of the

ellipse the expansion of the solid angle for small ϵ starts with ϵ^2.

$$\Omega(0,0,A) = \frac{F}{A^2}\left(1 - \frac{3}{4\pi}\frac{F}{A^2}(1+\frac{3}{2}\epsilon^2) + ...\right) \tag{13}$$

The case corresponding to Fig.6 is case number 4 which reads with the notation of Fig.7:

$$\Omega(p,0,h) = 2\int_0^{\phi_{max}} \int_{\theta_a(\phi)}^{\theta_b(\phi)} \sin\theta d\theta d\phi \tag{14}$$

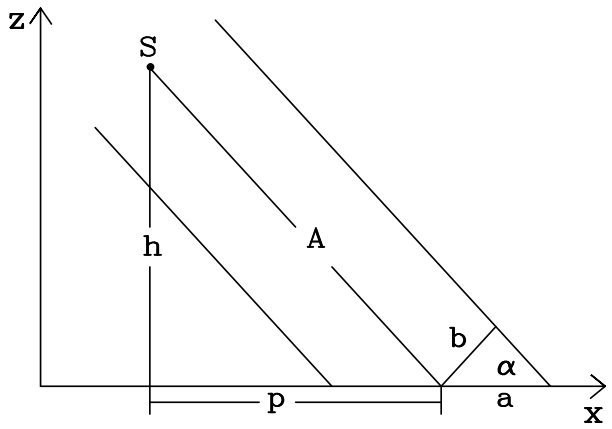

Figure 7: The larger principal axis a of the elliptical aperture cut at an angle α from the tube (see Fig.6) of radius b is along the x-axis of the coordinate system ($a = b/\sin\alpha$). The point source S(p,0,h) has the distance $A = \sqrt{p^2+h^2}$ from the center of the ellipse. The y-axis is alog the principal b-axis.

The integration limits ϕ_{max}, θ_a and θ_b are calculated from the relative position of the source and ellipse as shown in Fig.7.

$$\begin{aligned} \phi_{max} &= \arctan(b/\sqrt{p^2-a^2}) \\ \theta_a(\phi) &= \arctan((r_a(\phi)+r_b(\phi))/h), \quad \theta_b(\phi) = \arctan(r_a(\phi)/h) \end{aligned}$$

The $d\theta$ integration can again be accomplished

$$\begin{aligned} \Omega(p,0,h) &= 2\int_0^{\phi_{max}} d\phi\,(-\cos(\theta_b(\phi)) + \cos(\theta_a(\phi))) \qquad (15) \\ &= 2\int_0^{\phi_{max}} d\phi \left[1/\sqrt{1+\left(\frac{r_a}{h}\right)^2} - 1/\sqrt{1+\left(\frac{r_a+r_b}{h}\right)^2}\right] \end{aligned}$$

The functions r_a and r_b are complicated function of ϕ such that the integration over ϕ is done numerically.

$$
\begin{aligned}
r_a(\phi) &= \frac{pb^2\cos\phi - ab\sqrt{(b\cdot\cos\phi)^2 + (a^2-p^2)\sin^2\phi}}{(a\cdot\sin\phi)^2 + (b\cdot\cos\phi)^2} \\
r_b(\phi) &= \frac{2ab\sqrt{(b\cdot\cos\phi)^2 + (a^2-p^2)\sin^2\phi}}{(a\cdot\sin\phi)^2 + (b\cdot\cos\phi)^2}
\end{aligned}
$$

The numerical results show that the solid angle of a circle ($\alpha = \pi/2$, the result of Eq. 8) is by facor of 1.317 larger than the solid angle at $\alpha = \pi/4$ and independent of the distance A for $A/b \geq 8$ within the numerical precision.
The consequence is that the baseline with the same geometrical factor $geo = S_{max}/A$ has the same shape as the baseline for a circular aperture.

Table 1: The geometry factor *geo* is calculated for a point source moving with an amplitude $S_{max} = 0.1\,mm$ at 3 distances $A = 20, 40, 80mm$ and aperture areas $F_A = 25, 100, 200mm^2$. Note the decrease of *geo* with increasing aperture ($\propto F_A$) for a circle and the slight increase for a cone section at $\alpha = 45^o$ of a circular tube of area F_A.

	$A = 20mm$	$A = 40mm$	$A = 80mm$
$\frac{S_{max}}{A}$	$0.500 \cdot 10^{-2}$	$0.250 \cdot 10^{-2}$	$0.125 \cdot 10^{-2}$
circle			
$25mm^2$	$0.492 \cdot 10^{-2}$	$0.249 \cdot 10^{-2}$	$0.125 \cdot 10^{-2}$
$100mm^2$	$0.472 \cdot 10^{-2}$	$0.246 \cdot 10^{-2}$	$0.125 \cdot 10^{-2}$
$200mm^2$	$0.447 \cdot 10^{-2}$	$0.243 \cdot 10^{-2}$	$0.125 \cdot 10^{-2}$
square			
$25mm^2$	$0.493 \cdot 10^{-2}$	$0.249 \cdot 10^{-2}$	$0.125 \cdot 10^{-2}$
$100mm^2$	$0.472 \cdot 10^{-2}$	$0.246 \cdot 10^{-2}$	$0.125 \cdot 10^{-2}$
cone section ($\alpha = 45^o$)			
$25mm^2$	$0.507 \cdot 10^{-2}$	$0.251 \cdot 10^{-2}$	$0.125 \cdot 10^{-2}$
$100mm^2$	$0.520 \cdot 10^{-2}$	$0.254 \cdot 10^{-2}$	$0.125 \cdot 10^{-2}$

2.3 Solid angle of an extended circular source

2.3.1 Reciprocal property

The solid angle element $d\Omega$ at an isotropic radiating point source S subtended by an aperture element df_A

$$d\Omega \;=\; \frac{df_A \cdot \cos(\vartheta_{S,a})}{R_{S,A}^2}$$

with the distance $R_{S,A}$ between the position of the source and the surface element df_A and the angle $\vartheta_{S,A}$ between the direction $\vec{R}_{S,A}$ and the orthonormal of the surface element (see Fig.5). Accounting for the extension of the source the integral runs over the source area F_S and has to be normalized. Each surface element df_S is considered as an isotropic emitter in contrast to the Lambert's cosine law for diffuse radiators.
The typical geometry of parallel areas of source and aperture has the consequence that for each pair of area elements df_S and df_A the angle ϑ is the same on both sites such that $\cos(\vartheta_{A,S}) = \cos(\vartheta_{S,A})$. In these cases the integral can be written in the symmetrical form ($R_{S,A} = R_{A,S}$)

$$\frac{\Omega}{F_A} \;=\; \int_{F_S}\int_{F_A} \frac{df_A}{F_A}\frac{\cos(\vartheta_{S,A})}{R_{S,A}^2}\frac{df_S}{F_S} \tag{16}$$

Interchanging A and S the integral is the same so that the relation holds:

$$\frac{\Omega_S}{F_A} = \frac{\Omega_A}{F_S} \tag{17}$$

The starting situation when integrating first over F_A for a point source and then over the source area calculates Ω_S, that is Ω seen from the source.
This reciprocal property turns out to be useful especially for the calculation of cosine-smearing effects on the Mössbauer spectrum.

2.3.2 Circular aperture

The position of a point of the extended circular source of radius r_S at a distance $p \leq r_s$ from the center has the coordinate S(p,0,h). The solid

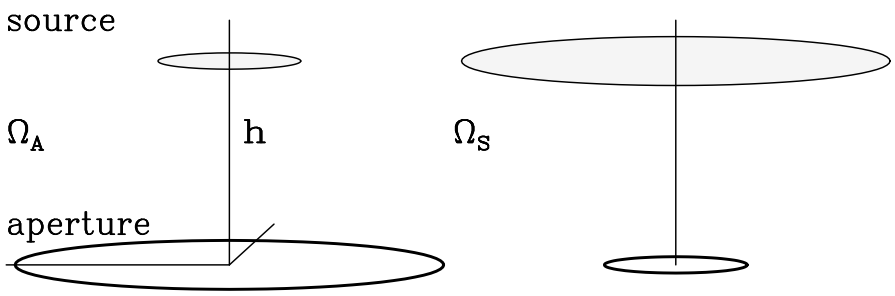

Figure 8: The two reciprocal geometries of circular source and aperture. On the left the small source of area F_S at hight h sees the aperture by the solid angle Ω_A and on the right the solid angle Ω_S subtended by the small aperture of the area of the source at the large radiating area of the size F_A.

angle subtended by a circular aperture at that point is given by [7]:

$$\begin{aligned} \Omega_A(p,0,h) &= 2\pi - \int_0^{2\pi} \frac{d\phi}{\sqrt{1+\left(\frac{r(\phi)}{h}\right)^2}} \qquad (18) \\ r(\phi) &= -p\cdot\cos\phi + \sqrt{(a\cos\phi)^2 + (a^2-p^2)\sin^2\phi} \end{aligned}$$

Integration over the source area reduces to an integration over p from $r = 0$ to $r = r_S$.

$$\Omega_A(h) = 2\pi \int_0^{r_S} \Omega_A(p,0,h) p dp \qquad (19)$$

This integration is performed numerically. For typical values of the velocity of $v_{max} = 8mm/s$ and frequency $\nu = 10Hz$ of the source the amplitude (triangular mode) $S_{max} = v_{max}/8/\nu$ becomes $0.1mm$. The parameter $geo = S_{max}/A$ for a point source at distance $h = A = 25mm$ from the aperture of circular shape has the value $geo = 0.4 \cdot 10^{-2}$. The effect of the extension of the circular source of $r_S = 2mm$ on the *geo*-parameter is shown in Table 2. With increasing radius of the aperture *geo* decreases by about 10% at $r_A = 10mm$. This deviation from $geo = S_{max}/A$ decreases rapidly with increasing distance A. The shape $\Omega(S(v))/Omega(S = 0)$ is very well preserved inserting an effective parameter *geo*.

Table 2: The geometry factor *geo* is calculated for an extended source of $r_S = 2.5mm$ at 3 distances $A = 20, 40, 80mm$ and aperture areas with radius from $F_A = 25, 100, 200mm^2$. Note the decrease of *geo* with increasing aperture ($\propto F_A$) for a circle and square and the slight increase for an ellipse at $\alpha = 45^o$. At $A \geq 80mm$ the size $r_S \leq 2.5mm$ has almost no effect on the parameter *geo*.

	$A = 28mm$	$A = 40mm$	$A = 80mm$
$\frac{S_{max}}{A}$	$0.400 \cdot 10^{-2}$	$0.250 \cdot 10^{-2}$	$0.200 \cdot 10^{-2}$
circle			
$25mm^2$	$0.487 \cdot 10^{-2}$	$0.248 \cdot 10^{-2}$	$0.125 \cdot 10^{-2}$
$100mm^2$	$0.468 \cdot 10^{-2}$	$0.246 \cdot 10^{-2}$	$0.124 \cdot 10^{-2}$
$200mm^2$	$0.445 \cdot 10^{-2}$	$0.242 \cdot 10^{-2}$	$0.124 \cdot 10^{-2}$
square			
$25mm^2$	$0.487 \cdot 10^{-2}$	$0.248 \cdot 10^{-2}$	$0.125 \cdot 10^{-2}$
$100mm^2$	$0.467 \cdot 10^{-2}$	$0.246 \cdot 10^{-2}$	$0.124 \cdot 10^{-2}$
ellipse ($\alpha = 45^o$)			
$25mm^2$	$0.501 \cdot 10^{-2}$	$0.250 \cdot 10^{-2}$	$0.125 \cdot 10^{-2}$
$100mm^2$	$0.514 \cdot 10^{-2}$	$0.253 \cdot 10^{-2}$	$0.125 \cdot 10^{-2}$

2.3.3 Quadratic aperture

The off-axis case of a point source has also been solved in [1]. Here the reciprocal property Eq. 17 shall be used. The solid angle subtended by the circular source at a point of the quadratic aperture is calculated in two steps. Eq. 19 cover the area $r_A \leq r_S$

$$\Omega_S(h, r \leq r_S) \;=\; 2\pi \int_0^{r_S} \Omega_S(p, 0, h) p dp$$

and the specialized Eq. 15 for $\alpha = \pi/2$ and $r = a = b$ the area $r_A > r_S$.

$$\begin{aligned} \phi_{max} &= \arctan(a/\sqrt{p^2 - a^2}) \\ \Omega_S(p, 0, h) &= \int_0^{\phi_{max}} d\phi \left[1/\sqrt{1 + \left(\frac{r_-}{h}\right)^2} - 1/\sqrt{1 + \left(\frac{r_+}{h}\right)^2} \right] \end{aligned}$$

The functions $r_\pm(\phi)$ become

$$r_\pm(\phi) \;=\; p\cos\phi \pm \sqrt{(a \cdot \cos\phi)^2 + (a^2 - p^2)\sin^2\phi}$$

The integration is again in two parts (see Fig.9)

$$\Omega_S(h, r > r_s) \;=\; 2\pi \int_{r_S}^{a/2} \Omega_S(p,0,h) p dp + 4 \cdot \alpha \int_{a/2}^{a/\sqrt{2}} \Omega_S(p,0,h) p dp$$

The angle $\alpha = \pi/2 - 2\beta$ is obtained from $a/2 = p\cos\beta$.

$$\Omega_A(h) \cdot F_A = \Omega_S(h, r \le r_S) \cdot F_S + \Omega_S(h, r > r_S) \cdot (a^2 - F_S) \qquad (20)$$

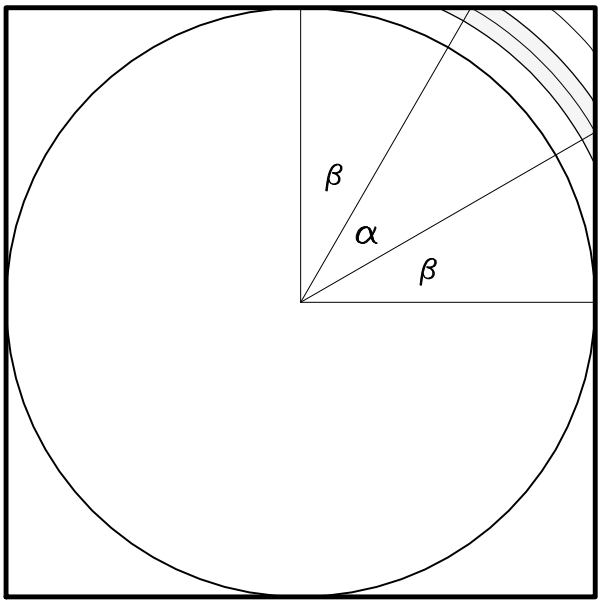

Figure 9: The squared area $F = a^2$ of the aperture is divided into a circular part up to the radius $r_A = a/2$ and the four remainder. The circular part is integrated by $df_A = 2\pi r dr$. For the remainder df_A reduces to 4 times the fraction given by $\alpha/2\pi$.

The calculated geometry effect for a square aperture with edge length of double the radius of a circular aperture is slightly smaller. The values of the parameter *geo* differ by few % (see Table 2).

2.3.4 Elliptical aperture of a cone section

The point source at point S in Fig.7 is replaced by a circular source of radius r_S orthonormal to the axis of the tube which is parallel to the line A in Fig.7. Using right handed unit vectors $\vec{e}_x, \vec{e}_y, \vec{e}_z$ the coordinates of a source point at distance $0 \le \rho \le r_S$ and angle ψ is given by

$$\begin{aligned} \rho\vec{e}_\rho &= \rho\,(\cos\psi\,\vec{e}_\xi + \sin\psi\,\vec{e}_y) \qquad (21) \\ \vec{e}_\xi &= \cos\alpha\,\vec{e}_x + \sin\alpha\,\vec{e}_z \end{aligned}$$

The (x,z)-plane is a mirror plane in Fig.7 with a point source and an extended circular source as well. The angle $\psi = 0$ in the mirror plane. A general point of the extended source

$$\vec{S}(\rho,\psi) = (-P + \rho\,\cos\psi\cos\alpha)\vec{e}_x + \rho\,\sin\psi\vec{e}_y + h\vec{e}_z \tag{22}$$

The more general case of Fig.7 with $\vec{S}(\rho,\psi)$ in the (x,y)-plane is treated by Mahmoud et al.[8] as the case of fig. 6 requiring the condition

$$\sqrt{(-P + \rho\,\cos\psi\cos\alpha)^2 + (\rho\,\sin\psi)^2} \geq a$$

which is fulfilled for $A > 2\,b/\sin 2\alpha + r_S$. The solid angle is calculated with the parameters $p = P - \rho\,\cos\psi\cos\alpha$ and $q = \rho\sin\psi$.

$$\Omega(p,q,h) = \int_{\phi_{min}}^{\phi_{max}} \int_{\theta_a(\phi)}^{\theta_b(\phi)} \sin\theta d\theta d\phi \tag{23}$$

The integration limits $\phi_{min}, \phi_{max}, \theta_a$ and θ_b are calculated from the relative position of the source and ellipse as shown in Fig.7.

$$\begin{aligned}
\phi_{min} &= \arctan\left(\frac{pq - \sqrt{b^2(p^2-a^2)+a^2q^2}}{p^2-a^2}\right)\\
\phi_{max} &= \arctan\left(\frac{pq + \sqrt{b^2(p^2-a^2)+a^2q^2}}{p^2-a^2}\right)\\
\theta_a(\phi) &= \arctan((r_a(\phi)+r_b(\phi))/h)\\
\theta_b(\phi) &= \arctan(r_a(\phi)/h)
\end{aligned}$$

The $d\theta$ integration can again be accomplished

$$\begin{aligned}
\Omega(p,q,h) &= \int_{\phi_{min}}^{\phi_{max}} d\phi\,(-\cos(\theta_b(\phi)) + \cos(\theta_a(\phi))) \qquad (24)\\
&= \int_{\phi_{min}}^{\phi_{max}} d\phi \left[1/\sqrt{1+\left(\frac{r_a}{h}\right)^2} - 1/\sqrt{1+\left(\frac{r_a+r_b}{h}\right)^2}\right]
\end{aligned}$$

The functions r_a and r_b are complicated function of ϕ such that the integration over ϕ is done numerically.

$$\begin{aligned}
r_a(\phi) &= \frac{pb^2\cos\phi + qa^2\sin\phi}{(a\cdot\sin\phi)^2 + (b\cdot\cos\phi)^2} - \frac{1}{2}r_b(\phi)\\
r_b(\phi) &= \frac{2ab\sqrt{(b\cdot\cos\phi)^2 + (a^2-p^2)\sin^2\phi + q\cos\phi(p\sin\phi - q\cos\phi)}}{(a\cdot\sin\phi)^2 + (b\cdot\cos\phi)^2}
\end{aligned}$$

The numerical results show that the solid angle of an ellipsis of a cone section of a tube of $6mm$ in diameter at $\alpha = \pi/4$ a source radius of $r_S = 2mm$ at a distance $A = 35mm$) is by facor of 1.59 larger than a circular aperture at the same distance (see Table 2). Although *geo* deviates considerably from $geo = S_{max}/A$ the shape of the baseline fits quite well ($< 1/10\sigma$ for 10^6 counts) with the larger value of *geo*.

3 Cosine smearing

The "cosine-smearing effect" is related to the geometry of the experimental setup. This effect leads to broadened lines with asymmetric shapes and shifts line centers outwards, particularly at higher velocities [13].

Crespo and Parellada [14] outlined in 1986: "The finite size of the Mössbauer absorber is taken into account to relieve geometrical conditions. An analytical expression reproducing quite accurately the actual shape of the resonant lines is derived. Deviations from the assumptions made have a small effect on line shape. The expression can easily be included in standard Mössbauer fitting routines to obtain accurate values of physical parameters even with bad geometrical conditions"

Flores-Llamas and Zamorano-Ulloa [15] considered Mössbauer line shape distortions due to finite dimensions of both the source and detector. "The effects of non-collimation of γ-rays and finite dimensions of source and detector upon the isomer shift, line broadening and line height of Mössbauer spectra have been determined by means of a two-dimensional angular distribution $f(r, \rho)$ that weights a Lorentzian line shape function. This distribution function, along with a few approximations, allow one to calculate, with ease, these Mössbauer spectral parameters. Our expressions, valid for finite dimensions, of source, detector and absorber, generalize previous calculations."

The numerical calculation developed in the following considers not only the shifts of the absorption lines of the superposed spectra but also their intensities diminished by the thickness effect increasing with the line shifts. Nevertheless there are approximations very elaborate to overcome. The emission and absorption of a polarized source and absorber, respectively, depend on the γ-direction so that the angular spread of the non-collimated γ-ray would require the calculation of the cross sections and the thickness effect for each direction.

The calculation is independent of any details of the theoretical spectrum (relaxation, distribution and other complexity).
Two apertures are considered, the circular one as a diaphragm or the quadratic detector surface, which is the typical shape of a pin-diode. First a solution is described for the case of a point source and afterwards

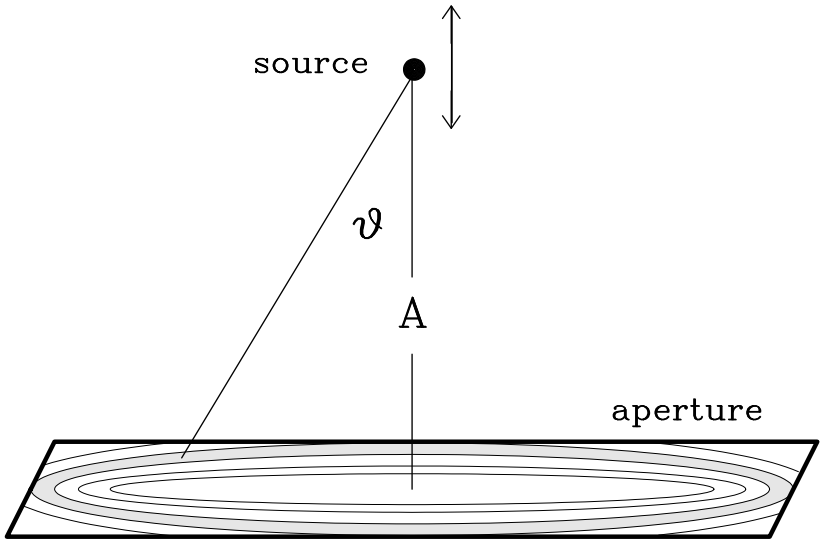

Figure 10: The angle α between the perpendicular of the square aperture and the direction from the point source to one of the circular rings (here the gray outer most complete circle) causes a reduced velocity (double arrow directions) by $\cos\alpha$. The distance between source and aperture is A.

the generalization for an extended source requiring much more computation time.

In a third step some simulations are presented which shall provide some limits of validity for the point source approximation and also an intrinsic approximation concerning the velocity dependence of the position of the source.

3.1 Area elements

There are many ways to choose the area elements df. Equidistant rings as in Fig.10 with sections $\Delta\varphi$ of the same area element df is an obvious choice. Fig.11 shows another choice of closely arranged circles which define uniformly distributed coordinates of the area elements. For both cases the total number of area elements can be extended to any approximation of the integral.
The first element is a circle of radius r at $(0,0)$ and area $df = \pi r^2$. In the first case ring radii R_i ($R_0 = r$) and angle sections $\Delta\varphi_i$ have to be calculated in order to get approximately equal area elements df. The coordinates of the elements are defined by (ρ,φ) with $\rho_i = (R_i + R_{i-1})/2$ in the middle of the ring from R_{i-1} to R_i. The R_i shall fulfill two

conditions:

$$\begin{aligned} n_i^\varphi \pi r^2 &= \pi R_i^2 - \pi R_{i-1}^2, \qquad n_i^\varphi \; integer \\ n_i^\varphi &\approx \frac{2\pi\rho_i}{R_i - R_{i-1}} \end{aligned} \tag{25}$$

The first condition determines the number n_i^φ of angular sections $\Delta\varphi_i$ by equal area elements. The second condition requires a shape of similar hight and width, namely $R_i - R_{i-1}$. Eliminating n_i^φ in a first step (as a non integer value)

$$\begin{aligned} \frac{2\pi(R_i + R_{i-1})/2}{R_i - R_{i-1}} &= \frac{\pi R_i^2 - \pi R_{i-1}^2}{\pi r^2} \\ r\sqrt{\pi} &= R_i - R_{i-1} \end{aligned}$$

such that integer value n_i^φ can be defined as the integer round off ν_i^φ

$$\begin{aligned} \nu_i^\varphi &= \sqrt{\pi}(R_i + R_{i-1})/r \quad and \\ \nu_i^\varphi &= \pi\frac{R_i + R_{i-1}}{R_i - R_{i-1}} \end{aligned}$$

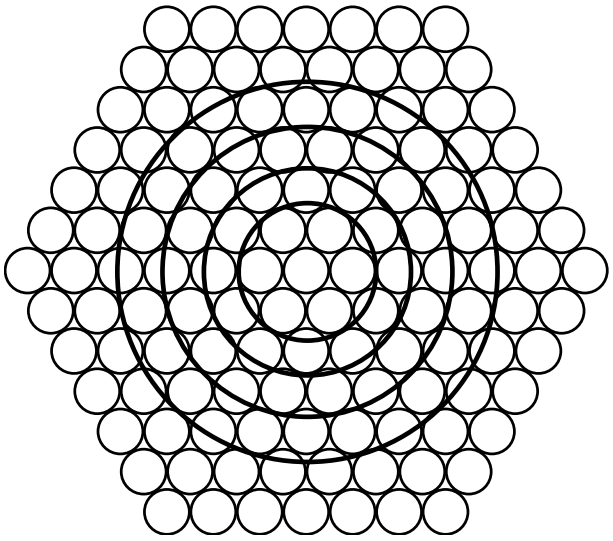

Figure 11: The integration area is covered with small circles of radius r which define a R, φ value at the center. The integration area of the large circle of radii $3r$, $(2\sqrt{3}+1)r$, $(2\sqrt{7}+1)r$, $(2\sqrt{13}+1)r$,... contain 7, 19, 37, 61,... small circles.

Starting with $R_1 = r$ and $R_0 = 0$ the integer $\nu_1^\varphi = \sqrt{\pi}$ is $n_1^\varphi = 1$. The

value of ν_2^φ is obtained step by step

$$\begin{aligned} \nu_2^\varphi &= \sqrt{\pi}(R_2+r)/r \quad and \quad \nu_2^\varphi = \pi\frac{R_2+r}{R_2-r} \\ \frac{R_2}{r} &= 1+\sqrt{\pi} \\ \nu_2^\varphi &= \sqrt{\pi}(2+\sqrt{\pi}) \end{aligned}$$

and gives $\nu_2^\varphi = 6.68$ such that $n_2^\varphi = 6$ inserted in the first Eq. 25 gives the value $R_2/r = \sqrt{7}$. This way table Tab.3 is obtained.

Table 3: The first 5 rings with $n_i^\varphi = floor(\nu_i^\varphi)$ area elements of size πr^2 and the total number $\sum_i$ are listed. $\Delta\varphi_i$ of ring $i > 1$ is $2\pi/n_i^\varphi$. At $\varphi_i^0 = \pm 2\pi/n_i^\varphi$ are the first and the last angle sectionsas a consequence of even n_i^φ-values.

i	R_i/r	ν_i^φ	n_i^φ	$\sum_i$
1	1	1	1	1
2	$\sqrt{7}$	$\sqrt{\pi}(2+\sqrt{\pi})$	6	7
3	$\sqrt{19}$	$\sqrt{\pi}(2\sqrt{7}+\sqrt{\pi})$	12	19
4	$\sqrt{37}$	$\sqrt{\pi}(2\sqrt{19}+\sqrt{\pi})$	18	37
5	$\sqrt{61}$	$\sqrt{\pi}(2\sqrt{37}+\sqrt{\pi})$	24	61
6	$\sqrt{91}$	$\sqrt{\pi}(2\sqrt{61}+\sqrt{\pi})$	30	91
7	$\sqrt{127}$	$\sqrt{\pi}(2\sqrt{91}+\sqrt{\pi})$	36	127

Interestingly, the total number of area elements $df = \pi r^2$ of the ring structure with the closed packed circles in Fig.11 is the same for the first 5 rings. However, the area enclosed by the outer ring in Fig.11 with a radius of $R = r(2\sqrt{13}+1)$ is by ≈ 6.4 area elements (= circle area) larger than for the ring structure of Tab.3. The fact that the n_i^φ up to i=7 have even values preserves the mirror symmetry with respect to the $\varphi = 0^o, 180^o$ axis as is the case in Fig. 11.

3.2 Point source

3.2.1 Absorber area orthonormal to the optical axis

The task to be solved is described by means of Fig.10. For each angle ϑ_i a spectrum is counted with a velocity scale $v_{max}^\vartheta = \cos\vartheta_i \cdot v_{max}$. The measured spectrum averages over all ϑ weighted by the solid angle belonging to the ring area $2\pi r\delta r$. The integrals of Eq. 20 for the solid angle of a squared and circular aperture are approximated by sums. The solid

Table 4: The (x, y)-coordinates of the circles of Fig.11 are tabulated for $x, y \geq 0$. The unit length is 1/2 the diameter of the circle.

x	0	1	2	3	4	5	6	7	8
y	0		0		0		0		0
		$\sqrt{3}$		$\sqrt{3}$		$\sqrt{3}$		$\sqrt{3}$	
	$2\sqrt{3}$		$2\sqrt{3}$		$2\sqrt{3}$		$2\sqrt{3}$		
		$3\sqrt{3}$		$3\sqrt{3}$		$3\sqrt{3}$			
	$4\sqrt{3}$		$4\sqrt{3}$		$4\sqrt{3}$				

angles for the N circular areas with the same angle ϑ according Fig.9 from $r_i - \Delta r$ to $r_i + \Delta r$ are per definition:

$$\begin{aligned} \Delta\Omega_{Ai} &= \frac{\pi(r_i + \Delta r)^2 - \pi(r_i - \Delta r)^2}{(A+S)^2 + r_i^2} \cos\vartheta_i \\ \cos\vartheta_i &= \frac{A+S}{\sqrt{(A+S)^2 + r_i^2}} \end{aligned}$$

The position of the source S(v) at velocity v which belongs to channel number k is given by Eq. 2 for the sinusoidal and Eq. 6 for the triangular case. Recalling Eq. 9 with the definition $A+S(v) = A(1+\delta(v))$ the solid angle $\Delta\Omega_{Ai}$ is written as:

$$\begin{aligned} \Delta\Omega_{Ai} &= \frac{2\pi r_i \Delta r}{A^2} \cos^3\vartheta_i(v) \frac{1}{(1+\delta(v))^2} \\ \cos\vartheta_i &= \frac{1+\delta(v)}{\sqrt{(1+\delta(v))^2 + (r_i/A)^2}} \end{aligned} \tag{26}$$

The sum over $\Delta\Omega_{Ai}(v)$ is only approximately equal to the solid angle $\Omega(S(v))$ of Eq.9 obtained by integration so that the terms of the sum have to normalized for each v by a factor $R(v)$.

$$R(v) \cdot \sum_i \Delta\Omega_{Ai}(v) = \Omega(S(v))$$

The normalization is necessary in order to preserve the geometry effect, the modulation of the baseline $\Omega(S(v))/\Omega(0)$, by the calculation of the cos-smearing.
The squared aperture (see Fig. 9) is treated the same way introducing the angular sections 4α instead of 2π in Eq. 26.

3.2.2 Absorber area tilted to the optical axis

The orientation technique for a series of single crystal measurements involves rotation of the crystal on a single-circle goniometer inclined at fixed angle α about an axis fixed in the crystal such that the γ-beam traces out a right (circular) cone in the crystal. Although the more complicated situation of Fig. 6 can be avoided by an extra aperture as shown in Fig. 12 the algebra is elaborated,

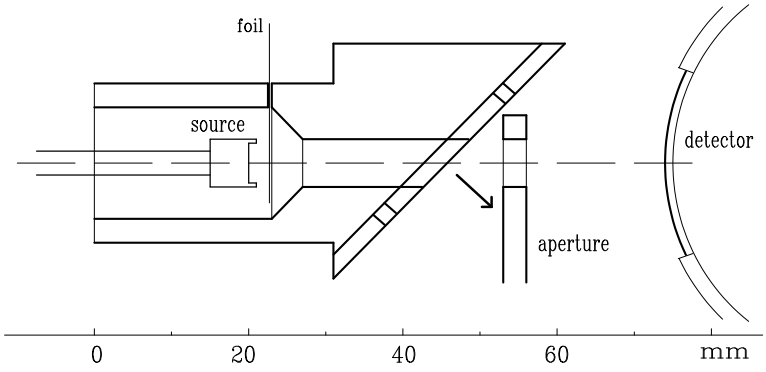

Figure 12: In order to avoid the more complicate situation of an elliptical shape of the aperture the configuration shown in Fig. 6 is improved by an extra circular aperture which has the diameter of the tube in front of the detector. The decrease of the solid angle can be reduced by a much shorter distance between source and cone section.

first since this thechnique was used several times and the data, which comprise a lot of measuring time, are still avaiable [4, 5, 16]. The evaluation of the electic field gradient (EFG) together with the mean square displacement MSD-tensor by a simultaneous fit of 19 spectra is a challenge, especially the comparison with the published results obtained by point by point fits of the spectra. A second reason can be the decrease of the solid angle by the extra aperture which distance to the source is necessarily increased.

The area of the cone section at an angle α is enlarged by the factor $1/\cos\alpha$. This area is covered by ellipses with an enlarged main axis by the same factor as shown in Fig. 14 so that there are the same number of area elements $\pi r{\cdot}r/\cos\alpha$. The coordinates of the centers of the ellipses in the (x,y,z)-system are the (x,y) coordinates of the corresponding circles in the (x,y)-plane and in the tilted (x,y')-plane with the rotated unit vector

$$\vec{e}_\xi \;=\; \cos\alpha\vec{e}_x + \sin\alpha\vec{e}_z$$

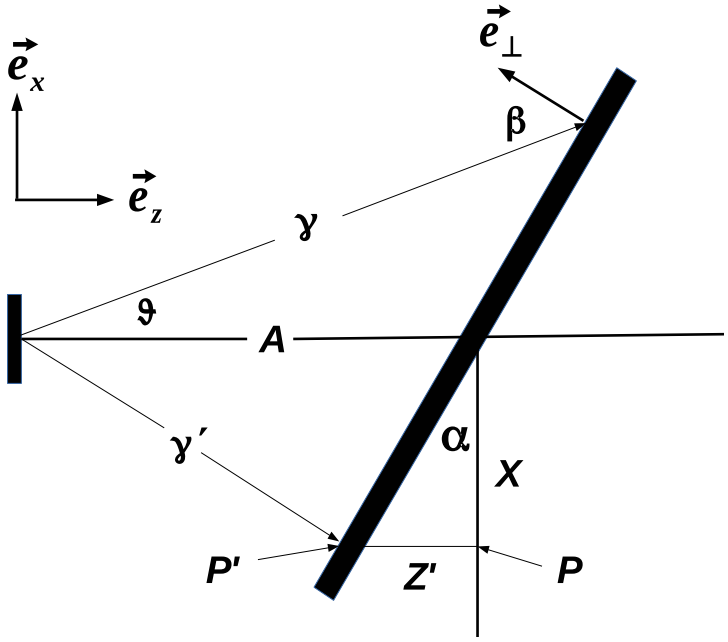

Figure 13: The source on the left, the absorber is tilted around the y-axis clockwise by an angle α. Two γ-direction γ and γ' are shown. Direction γ includes the angle ϑ with the z-axis and leads to a decrease of the doppler velocity by $\cos\vartheta$. The angle β determines the solid angle of the area element of the absorber. The center of the absorber is at $A\vec{e}_z$. The point P in the (x,y)-plane at $\phi = \pi$ the surface element of the tilted absorber at P' has the z-coordinate $A + x\tan\alpha$. The surface element at P' is enlarged by the factor $1/\cos\alpha$.

a z-component has to be added the length of which is $x\tan\alpha$ such that the ellipse number i has the position

$$\vec{r_i} \;=\; r\cos\phi_i\vec{e}_x + r\sin\phi_i\vec{e}_y + A\vec{e}_z + r\cos\phi_i\tan\alpha\vec{e}_z$$

in the (x,y,z)-system. The solid angle $\Delta\Omega_{Ai}$ at the position (0,0,0) of the source subtended by the ellipse at $\vec{r}_i$ becomes

$$\begin{aligned}\Delta\Omega_{Ai} &= \frac{\pi r^2/\cos\alpha}{|\vec{r}_i|^2}\cos\beta_i \qquad (27)\\ \cos\beta_i &= \frac{\vec{e}_\perp(-\vec{r}_i)}{|\vec{r}_i|}\end{aligned}$$

$\vec{e}_\perp$ is the unit vector orthonormal to the (x,y')-plane.

$$\vec{e}_\perp \;=\; \sin\alpha\vec{e}_x - \cos\alpha\vec{e}_z$$

The solid angle element finally becomes:

$$\Delta\Omega_{Ai} = \frac{\pi r^2 A}{|\vec{r}_i(v)|^3} \tag{28}$$

The sum over $\Delta\Omega_{Ai}(v)$ is only approximately equal to the solid angle $\Omega(S(v))$ obtained by the integral of Eq. 15. The angle ϑ is given by

$$\begin{aligned} \cos\vartheta &= \frac{\vec{e}_z \vec{r}_i(v)}{|\vec{r}_i(v)|} \\ &= \frac{A + r\cos\phi_i \tan\alpha}{|\vec{r}_i(v)|} \end{aligned} \tag{29}$$

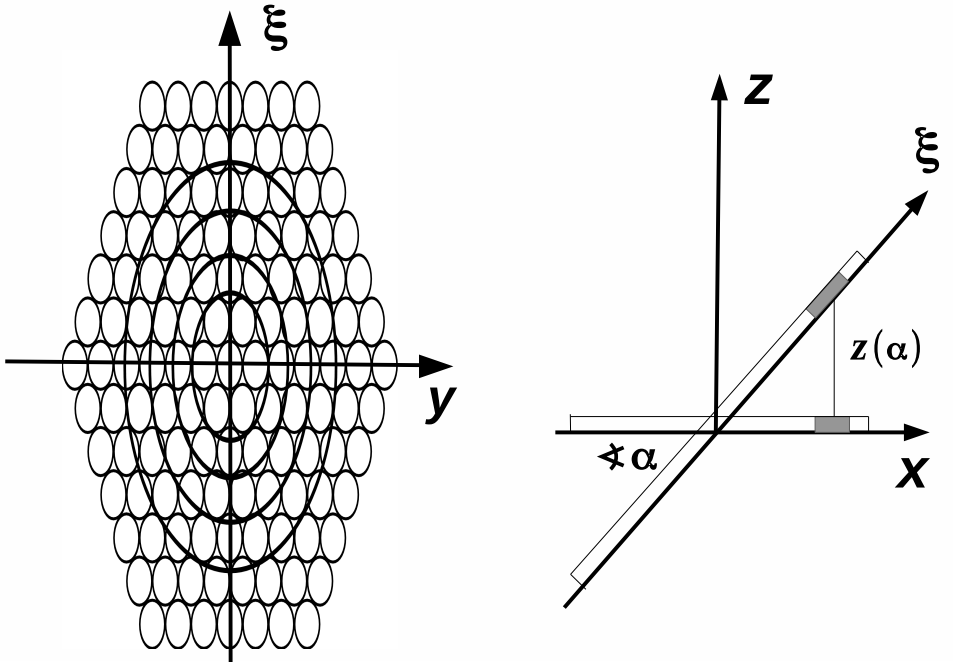

Figure 14: The area shown in Fig. 11 is tilted around the y-axis by the angle α between the x- and ξ-axis and adapted to the conic section of the geometry shown in Fig. 6 covered by ellipses. The principal axes of the ellipses in y-direction are that of the circles and in ξ-direction are multiplied by $1/\cos\alpha$. The position of the ellipses in the x, ξ-plan have the same (x,y)-coordinates, the z-coordinates are shifted to $z(\alpha) = x\tan\alpha$ as indicated on the left side. This choice preserves the summation algorithm used for the circles of Fig. 11.

3.3 Extended source

The integrals over df_S of the source and df_A of the aperture in Eq. 16 have to be evaluated by a double sum storing each pair product $df_S \cdot df_A$

together with $\cos\vartheta$ of the angle ϑ between the vector from df_S to df_A. The solid angle and the effective velocity decrease by the same factor $\cos\vartheta$. In case of the tilted absorber the situation is more complicated as the solid angle decreases by the cos of another angle β (see Sec.3.2.2).
For each member of the double sum a spectrum is calculated. The sum of these spectra represent the theoretical spectrum to be compared with the experimental one.
In order to minimize the number of spectra the symmetry of the geometry shall be accounted for.
Only sources with rotational symmetry are considered. The usual case of a source smaller than the aperture suggest first to sum over the source from a point of the aperture which by the rotational symmetry of the source has a manifold of equivalent points, the ring sections of Fig.10.
The arrays of $\Delta\Omega$ and $\cos\vartheta$ have N members in case of a point source counting the rings and partial rings at the corners of squared apertures (/detectors). The integral over the source (replace by a sum up to 61 area elements) is the same from all points on a ring obvious by the rotational symmetry of the source. Eq. 16

$$\begin{aligned}\frac{\Omega_S}{F_A} &= \int_{F_A}\frac{df_A}{F_A}\int_{F_S}\frac{\cos(\vartheta_{S,A})}{R^2_{S,A}}\frac{df_S}{F_S}\\ \Omega_S &= \frac{1}{F_S}\sum_{N_A} df_A \sum_{N_S} df_S \frac{\cos(\vartheta_{S,A})}{R^2_{S,A}}\end{aligned}$$

The double sum shall be evaluated in detail. The vectors in the plane of the source and aperture are $\vec{\rho_k}$ and $\vec{r_i}$, respectively.

$$\begin{aligned}\vec{r_i} &= (r_i\cos\phi_i, r_i\sin\phi_i, A)\\ \vec{\rho_k} &= (\rho_k\cos\phi_k, \rho_k\sin\phi_k, 0)\end{aligned}$$

The vector $\vec{R_{i,k}} = \vec{r_i} - \vec{\rho_k}$ points from surface element df_{Sk} to df_{Ai} and forms an angle $\vartheta_{i,k}$ with the z-axis which is parallel to the velocity directions.

$$\begin{aligned}\cos\vartheta_{i,k} &= \frac{A}{|\vec{r_i} - \vec{\rho_k}|}\\ &= \frac{A}{\sqrt{A^2 + r_i^2 + \rho_k^2 - 2r_i\rho_k\cos(\phi_k - \phi_i)}}\end{aligned}$$

The integrand of the integral $\int_0^{2\pi} d\phi_k$ over the source ring

$$\frac{\cos\vartheta_{i,k}}{R^2_{i,k}} = \frac{A}{\sqrt{A^2 + r_i^2 + \rho_k^2 - 2r_i\rho_k\cos(\phi_k - \phi_i)}^3}$$

is independent of the angle ϕ_i (obvious by variable substitution $d\phi_k$ to $d(\phi_k - \phi_i)$). The rotational symmetry is, of course, only approximated by the sum substituting the integral.
The integration over the aperture with area elements $df_{Ai} = r_i dr_i d\phi_i$ can be replaced by $df_{Ai} = 2\pi r_i dr_i$. Following the convention leading to Eq. 26 the solid angle

$$\Delta\Omega_{Si} = \frac{4\pi r_i \Delta r}{A^2} \sum_{k=1}^{N_s} \frac{df_{Sk}}{F_S} \cdot \cos^3 \vartheta_{i,k}(A, r_i, \rho_k, \phi_k)$$

belongs to N_s spectra with $v_{max}^{\vartheta} = \cos\vartheta_k \cdot v_{max}$. The area elements $df_{Sk} = \pi r^2$ are independent of k and equal to the small circle area, such that F_S/df_{Sk} is just the number of area elements N_S. The N_S spectra are of equal weight df_{Sk}/F_S, their sum is averaged by the factor $1/N_S$. The area and the area elements drop out of the calculation. How closely the area elements cover the source area (see Fig.11) comes not into play only their coordinates.

The position of the source is introduced changing the distance A to $A + S = A(1 + \delta(v))$.

$$\Delta\Omega_{Si}(v) = \frac{4\pi r_i \Delta r}{A^2} \frac{1}{N_S} \sum_{k=1}^{N_s} \cos^3 \vartheta_{i,k}(\delta(v), r_i, \rho_k, \phi_k) \frac{1}{(1 + \delta(v))^2} \qquad (30)$$

The N_A ring areas of an circular aperture give an array of N_A solid angle elements $\Delta\Omega_{Sk}$ and an array of dimension $N_A \cdot N_S$ of $\cos\vartheta_{i,k}$ functions. The r_i and Δr are calculated for a circular aperture of radius R_A:

$$\Delta r \;=\; \frac{R_A}{2N_A}, \qquad r_i = \Delta r(1 + 2i)$$

In case of quadratic aperture the corners have to be added to the arrays according to Fig.9. The $\Delta\Omega_{Ak}$ are the calculated by use of Eq. 20.
As argued for the point source (Eq.26) the $\Delta\Omega_{Ak}$ have to be normalized by $\Omega_{Ak}(0)$, the solid angle at source position $S = 0$.

3.4 Approximtion of the velocity dependence

3.5 Reduction of cosine arrays

3.6 Cosine thickness correction

The γ-ray deviating from the otical axis is not only modulated by a changed maximal velocity $\cos\vartheta \cdot v_{max}$ but also by an increase of the

thickness of the absorber. The thickness t of the absorber increases to $t/\cos\vartheta$. The small correction $t \cdot (1+\epsilon)$

$$\begin{aligned} t \cdot (1+\epsilon) &= t/\cos\vartheta \\ \epsilon &= 1/\cos\vartheta - 1 \end{aligned}$$

has to be calculated for each velocity channel of the theory.

In order to calculate a correction proportional to ϵ the equations of the forward scattering theory (see [17]) are expanded to terms linear in ϵ. The resonant part ($\propto f$ -factor) of the source spectrum is the sum of Lorentzians multiplied by the 2x2 density matrices r_i:

$$\begin{aligned} \rho_S(E) &= \frac{2}{\Gamma\pi}\sum_i \frac{1}{2} r_i \cdot \frac{(\Gamma/2)^2}{(E-E_i)^2+(\Gamma/2)^2} \qquad (31) \\ 1 &= Tr\left(\sum_i \frac{1}{2} r_i\right) \\ \begin{pmatrix} 1/2 & 0 \\ 0 & 1/2 \end{pmatrix} &= \int_{-\infty}^{\infty} \rho_S(E) dE \end{aligned}$$

The total intensity of the resonance part, sum over all Lorentzians, is normalized to 1. Γ is the natural line width. Since the Lorentz function is real and the density matrix r_i of a transition is hermitian, the diagonal elements of $\rho_S(E)$ are real numbers. If the source is moving with velocity v the energies E_i are shifted by the Doppler effect to $E_i(1+v/c)$ such that $\rho_S(E,v)$ is a function of E and v.

The radiation travels through a material of refraction index $\mathbf{n}(E)$:

$$\mathbf{n} = \underline{1} - \frac{\sigma f(\mathbf{k})}{2k}\sum_j N_j \sum_i r_i^j \cdot \frac{\Gamma/2}{E - E_i^j - i\Gamma/2} - i\kappa/2\underline{1} \qquad (32)$$

with the unit 2x2 matrix $\underline{1}$, the cross section σ, the Lamb-Mössbauer factor f in direction $\mathbf{k}$, N_j of nuclei of type j with density matrix r_i^j and the non-resonant absorption coefficient κ due to all oscillators far from resonance. The density matrix at position z (traveling from 0 to z) is given by

$$\rho(E,z) = e^{-i\mathbf{n}kz}\rho_S(E)e^{+i\mathbf{n}^\dagger kz} \qquad (33)$$

Eq. 32 shall be split in a scalar part $\mathbf{n}_1$ proportional to the unit matrix $\underline{1}$ and a traceless 2x2 matrix $\mathbf{n}_2$. Only $\mathbf{n}_2$ depends on the polarization of the absorber.

$$\begin{aligned}
\mathbf{n}(E) &= (\mathbf{n}_1(E) - i\kappa/2) \cdot \underline{1} + \mathbf{n}_2(E) \\
\mathbf{n}_1 &= 1 - \frac{\sigma f(\mathbf{k})}{2k} \sum_{j,i} N_j \frac{1}{2} Tr(r_i^j) \cdot \frac{\Gamma/2}{(E - E_i^j) - i\Gamma/2} \\
\mathbf{n}_2 &= -\frac{\sigma f(\mathbf{k})}{2k} \sum_{j,i} N_j \left(r_i^j - \frac{1}{2} Tr(r_i^j) \right) \frac{\Gamma/2}{(E - E_i^j) - i\Gamma/2}
\end{aligned}$$

The density matrix of Eq. 33 shall be expressed by $\mathbf{n}_1$ and $\mathbf{n}_2$ written as a product of three factors.

$$\begin{aligned}
\rho(E, v, t) &= e^{-i((\mathbf{n}_1 - i\kappa/2)\underline{1} + \mathbf{n}_2)kt} \rho_S(E) e^{+i((\mathbf{n}_1 - i\kappa/2)^\dagger \underline{1} + \mathbf{n}_2^\dagger)kt} \\
&= e^{-\kappa kt} e^{-i(\mathbf{n}_1 - \mathbf{n}_1^*)kt} \cdot e^{-i\mathbf{n}_2 kt} \rho_S(E, v) e^{+i\mathbf{n}_2^\dagger kt} \\
&= e^{-\kappa kt} \rho_1(E) \rho_2(E, v)
\end{aligned}$$

The first two factors are scalars. The third factor $\rho_2(E, v)$ depends on $\mathbf{n}_2$ which vanishes for an unpolarized absorber and $\rho_2(E, v)$ reduces to $\rho_S(E, v)$.

The counts of the Mössbauer spectrum are a sum of three contributions,

$$\begin{aligned}
N(v) &= N_M f_S \int_{-\infty}^{+\infty} Tr(\rho(E, v, z)) dE \\
&\quad + N_M (1 - f_S) e^{-\mu_m t} \\
&\quad + N_{background} e^{-\mu_b t}
\end{aligned} \tag{34}$$

the resonance part f_S of the source calculated by the convolution integral of the trace of the density matrix, the non-resonance part $(1 - f_S)$ only attenuated by electronic absorption ($\mu_m = \kappa k$) and the electronic absorption of the background radiation with an absorption coefficient μ_b. Using $\rho(E, v, t) = e^{-\kappa kt} \rho_1(E) \rho_2(E, v)$ from above

$$\begin{aligned}
N(v) &= N_M e^{-\mu_m t} \left(f_S \int_{-\infty}^{+\infty} \rho_1 Tr(\rho_2) dE + (1 - f_S) \right) \\
&\quad + N_{background} e^{-\mu_b t}
\end{aligned}$$

the attenuation of γ-radiation of the Mössbauer transition becomes a common factor $N_m = N_M e^{-\mu_m t}$. The attenuation of the background

$N_{background}$ passing the absorber $N_{bg} = N_{background}e^{-\mu_b t}$ can be neglected in most cases.

At $z = t(1+\epsilon)$ Eq. 33 and the background radiation is expanded to linear term of ϵ:

$$\begin{aligned} \rho(E,v,z) &= (1 - \epsilon\,\kappa kt - \epsilon\,kti(\mathbf{n}_1 - \mathbf{n}_1^*))\,\rho(E,v,t) \\ &\quad -\epsilon\,kti\left(\mathbf{n}_2\rho(E,v,t) - \rho(E,v,t)\mathbf{n}^\dagger{}_2\right) \\ N_{bg}(z) &= (1 - \epsilon t\mu_b)N_{bg}(t) \end{aligned} \tag{35}$$

The property that $e^{-i\mathbf{n}kt}$ and $\mathbf{n}$ commutes has been used. $N(v,\epsilon) \equiv N(v, t(1+\epsilon))$ at $t(1+\epsilon)$ in Eq. 34 is expressed by $N(v,0)$ and a term proportional to ϵ. The counts N_M of the Mössbauer transition are attenuated passing the absorber by non-resonant absorption to $N_m = N_M e^{-\kappa kt}$. This attenuation $e^{-\mu_m t}$ is a common factor for all contributions, resonant and non-resonant absorption, such that the ratio of the measured background $N_{bg} = N_{background}e^{-\mu_b t}$ passing the absorber $N_{gb}/(N_m + N_{gb})$, the background fraction $bg_{fraction}$, is a well defined number of the spectrum. The alteration of thickness $t(1 + \epsilon(\theta))$ by the angle θ leads to a dependence of the $bg_{fraction}$ on the γ-direction from a source area element to an absorber area element.

$$\begin{aligned} N(v,\epsilon) &= N(v,0) - \epsilon t\mu_b N_{bg} \\ &\quad -\epsilon t \cdot \kappa k N_m \left(f_S \int_{-\infty}^{+\infty} \rho_1 Tr(\rho_2) dE + (1 - f_S)\right) \\ &\quad -\epsilon t \cdot ikN_m \cdot f_S \int_{-\infty}^{+\infty} (\mathbf{n}_1 - \mathbf{n}_1^*)\,\rho_1 Tr(\rho_2)\,dE \\ &\quad -\epsilon t \cdot ikN_m \cdot f_S \int_{-\infty}^{+\infty} \rho_1 Tr\left(\mathbf{n_2}\rho_2 - \rho_2\mathbf{n_2^\dagger}\right) dE \end{aligned} \tag{36}$$

The ϵt-terms start with the decrease of the background N_{bg}. The first of the three convolution integrals is calculated to obtain the spectrum at thickness t (Eq. 35). Here it appears to correct for the increase of non-resonant absorption with increasing thickness. For an unpolarized absorber the contribution $\mathbf{n_2}$ to the index of refraction is a zero 2x2 matrix. In that case only one further convolution integral has to be calculated, which corrects for the increased resonant absorption with increasing thickness ϵt. The case of an polarized absorber is by the third convolution integral only approximately captured. $\mathbf{n_2}$ and also $\mathbf{n_1}$

depend on the γ-direction with respect to the orientation of the absorber (single crystal) which slightly differ not only for each ϑ- but also the φ-angle of the area element of absorber and source.
The theory curve $th(v) = \sum_{i,k} N(v, \epsilon(\vartheta_{i,k}))/\overline{a}$ is normalized to the unit areas of source and aperture by some constant $\overline{a}$, such that $N(v = \infty, 0)$ remains unchanged. $N(v = \infty, 0)$, however, is not any more equal to $th(v = \infty)$ since the electronic absorption factored in decreases $th(v = \infty)$. To be comparable with the baseline of the experimentel counts $th(v)$ has to be readjusted to $Th(v)$

$$\begin{aligned} Th(v) &= th(v)/th(v = \infty) \qquad (37) \\ th(v = \infty) &= \frac{1}{\overline{a}} \sum_{i,k} bg_{fraction} \epsilon(\vartheta_{i,k}) \mu_b - (1 - bg_{fraction}) \epsilon(\vartheta_{i,k}) \mu_m \end{aligned}$$

3.7 Simulations

All simulations have been done using the convolution integral with a source of natural line width $\Gamma_N = 0.097 mm/s$, a Lamb-Mössbauer factor 0f 0.7 and setting the background fraction to $bg_{fraction} = 0.2$. There are two possibilities to generate "experimental" spectra. Simulating the counting process by an algorithm [18], which transforms a uniform random variable $u \in (0,1)$ to a rate $\lambda = counts/s$ of a Poisson process. The time consumption is much less using of the cumulative distribution function (CDF) valid in the limit of the normal distribution of large numbers of accumulated counts $C(channel = k)$. The experimental spectrum points $C(k)$ are calculated by the inverted CDF [19] $\Phi(u)$ of a random number $u \in (0,1)$: $C(k) = \sqrt{th(k)} \cdot \Phi^{-1}(u)$. For the inverted CDF $\Phi^{-1}(u)$ the approximation AS70 of Odeh and Evans (1974) [12] is applied.

The line position and the thickness correspond to the line at negative velocities and the effective thickness of a 25μ α-iron foil at RT (Lamb-Mössbauer factor f=0.8). The baseline has been set to 10^6 counts and all χ^2 values refer to 512 channels around the position of $-5 mm/s$ such that the 1 σ standard deviation of χ^2 becomes $\sigma_{\chi^2} = \sqrt{2/512} = 0.088$. The most accurate theory is calculated with 10 rings for the circular and 15 rings for the square aperture and 61 (= 5 rings of Fig. 11) area elements for the extended source. This means up to $15 \cdot 61 = 915$ spectra have to be superposed. The "true" experimental counts are obtained from this spectrum with a χ^2-value close to 1. The calculation of the spectrum with a single line which shall be considered in the following takes about $0.2s$ using a 2GHz processor. The first check of the accuracy of the theory is done reducing the number of superposed spectra. 6 rings and 9 rings for the circular and square aperture, respectively, together with 19 (Tab. 3) area elements of the extended source increases the χ^2-value by about $1/3\,\sigma_{\chi^2}$ in case of the geometry used to calculate the spectra of Fig. 16.

Fig. 15 demonstrates the cosine-smearing effect. In order to show up this effect extreme dimensions of the geometry are chosen, a circular/square aperture of $20mm$ in diameter/edge length at a distance of only $25mm$ from a point source. For the circular aperture 6 ring elements give the superposition of 6 spectra with linearly (with radius r) increasing inten-

sity shifted to higher velocities from $v_p = -5mm/s$ to $v_p + v_p/\cos\vartheta_r$. For the outer ring the ϑ_r-angle a value of $\tan\vartheta = 10mm/6 \cdot 5.5/25mm$ (see Fig. 10 and also Fig. 9) gives a shift of $0.326\,mm/s$. With a much smaller line width of $0.005mm/s$ 5 lines become visible in Fig. 15 on the left. The spectrum of the first ring $r = 10mm/6$ is almost unshifted and not resolved from the spectrum of the second ring. The square aperture which is realized in case of pin-diodes (aperture is the detector area) with its outer ring sections as shown in Fig. 9 adds spectra with decreasing intensities with further increasing shifts. Preserving the value of $\Delta r = 10mm/6$ three r-values from $10mm$ to $10mm \cdot \sqrt{2}$ are defined which intensities decrease with increasing radius to edges of the square.

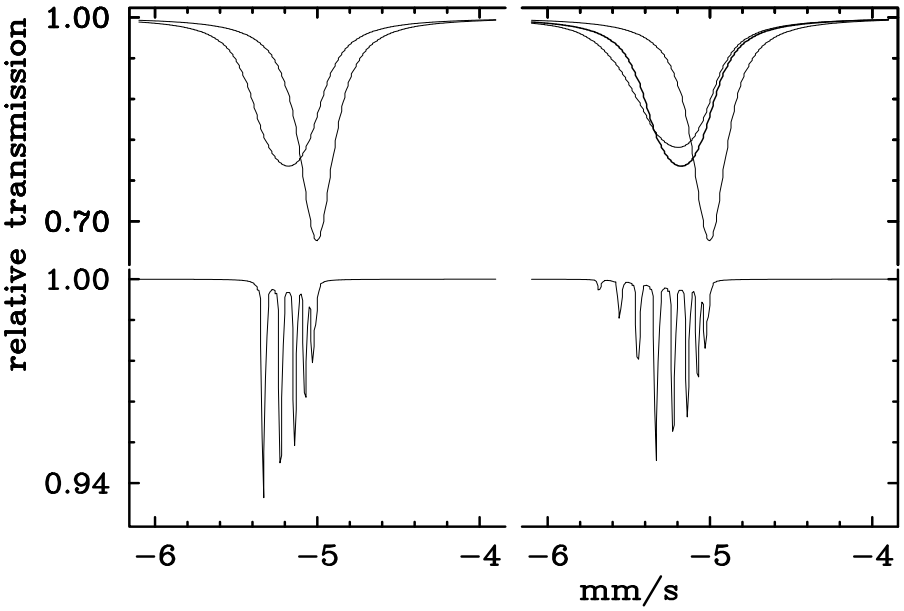

Figure 15: On both sites, left and right, the absorption line at $-5mm/s$ calculated with an effective thickness of $t_{eff} = 4$ and natural line width ($\Gamma_N = 0.097mm/s$) is plotted for three cases using an ideal point source: The absorption line at infinite distance from the aperture, and the lines at a distance of $25mm$ from a circular aperture of a diameter of 20mm shown on the left and a square aperture of the same edge length on the right side on the upper half of the figure. In order to visualize the different shapes obtained with a circular aperture and square aperture the former one is also plotted on the right side as a third absorption line. The lower half of the figure shows the superposition of the absorption lines (6 and 10, respectively) with narrow line width which has been set to $\Gamma_N/20$.

Fig. 16 demonstrates the influence on the shape of the absorption line by stepwise neglect of the thickness effect of electronic absorption and the extension of the source.

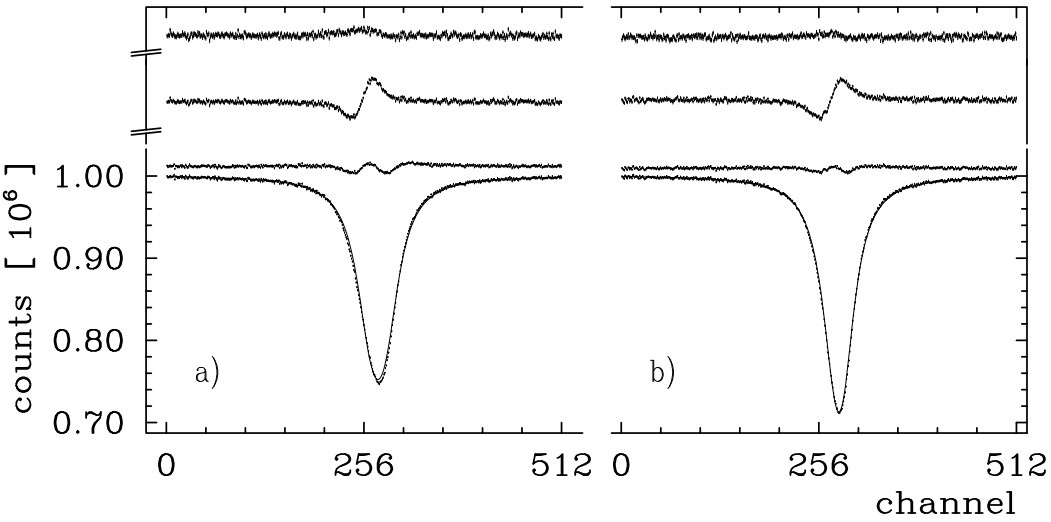

Figure 16: The single line at position $-5mm/s$ and an effective thickness of 4.0 corresponding to the lines 5,6 of a 25μ thick α-iron foil is calculated for the geometry of an ideal source of 5mm diameter at a distance of $25mm$ to a circular aperture (Fig. a)) of $16mm$ in diameter ($2cm^2$) and a square aperture of $10mm$ edge length (Fig. b)). A baseline 10^6 counts has been simulated according to Poisson statistics such that χ^2 is close to 1. The first 512 of 2048 channels are plotted. Three steps of approximations are shown. The residual spectra on top are obtained neglecting the electronic absorption $\mu_t = 1.2875$ of iron ($0.0515/\mu$), the next below reduces further to a point source, and the third one belongs to a fit of the absorption line below with effective parameters. For the circular aperture a) the $\chi^2 = 5.7$ is large with a thickness $t_{eff} = 3.55$ instead of 4, position $-5.0017mm/s$ ($-5mm/s$) and an increased line width $1.333\Gamma_N$ are obtained. Although the approximation by a point source gives residual spectra of similar deviations in a) and b) the $\chi^2 = 1.7$-value is much smaller and the effective parameters are closer to the true one ($t_{eff} = 3.69$, $-5.0068mm/s$, and $1.225\Gamma_N$).

The definition of limits of the geometry where the cosine-smearing effect becomes small enough to be neglected is linked to the acceptable χ^2-value which depends on the number of collected counts. If the theory model is far from the measured spectrum such that χ^2 is large ($\chi^2 - 1 >> \sigma_{\chi^2}$) and increases with increasing number of counts the neglect of cosine-smearing and point source approximation is indicated. At larger distances between source and aperture/detector theses effects become negligible. In Fig. 17 the distance is doubled to $50mm$ and the effect calculated for a squared aperture of $1cm$. The geometry corresponds to a distance of $80mm$ for a $1.6cm$ sized absorber as a circular aperture. It is shown that χ^2 increases only by 1 σ_{χ^2}. This means that the aim of a fit of $\chi^2 \approx 1$ cannot be reached for an exact(=true) theory.

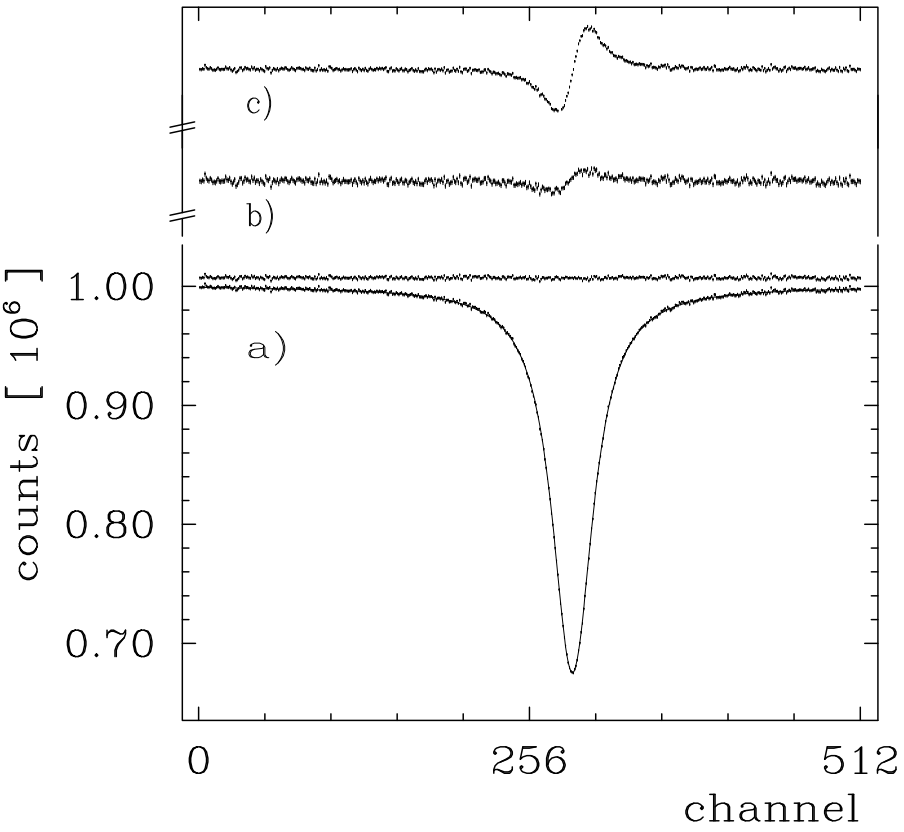

Figure 17: The single line is simulated at position -5mm/s, an effective thickness of 4.0 (see Fig. 16), an ideal source of $5mm$ in diameter, and a square aperture of $10mm$ edge length at a distance of 50mm. Fig. a) shows the fitted absorption line without electronic absorption and a point source. χ^2 is close to 1, the slight increase is much smaller than σ_{χ^2}. The neglect of the electronic absorption has a negligible effect on χ^2. Fig. b) is the residue before the fit. Complete neglect of cosine-smearing (source at infinity) produces a residue of Fig. c). Fitting under this condition increase χ^2 by about $\sigma_{\chi^2} = 0.088$. The effective parameters of the two fits are very similar: $t_{eff} = 3.95(3.94)$, $-5.0028mm/s(-5.0190)$, and $1.023\Gamma_N(1.053\Gamma_N)$. The effective values for the source at infinite distance are in brackets.

4 Calibration of the velocity scale

The calibration of the velocity scale of the Mössbauer spectrum is a prerequisite for a reliable evaluation of the experimental spectra, especially concerning line positions and their widths. The standard method is the determination of the line positions of an α-iron absorber on the channel scale and calculating the mm/s per channel by the known overall splitting of the iron absorber or the average of the three splittings (1,6),(2,5) and (3,4). The Fit;o)- Mössbauer spectrum fitting program takes the unfolded spectrum and the appropriate average of the 12 absorption lines [20]. In WMOSS4 [21] a simple interpolation by the best straight line fitted to the peak positions is offered. The fit-program NORMOS [22] interpolates using a cubic spline between the first and the last velocity value. Other programs [23, 24, 25, 26, 27, 28, 29] do not handle the non-linearity of the velocity scale. The fit of the calibration spectrum stops at some local minimum where the position of the more intense absorption lines (1 and 6 in case of $\alpha - Fe$) have the higher weight for the scaling factor.
The linearity error for driving units in the triangular mode is guaranteed to be $< 0.15\%$ at the resonance frequency by WISSEL [30], which still corresponds to more than one channel in 10^3. Using optimal soft springs an error less than 0.5% can be promised by FASTCOMTEX [31].

A more accurate calibration of the velocity scale of a Mössbauer spectrum can only be obtained with a more elaborate correction function for the non-linearity of the driving unit. Several functions based on a Fourier expansion are constructed to get a fit over a large velocity range to both halfs of the MCS-spectrum.

4.1 Velocity to channel

4.1.1 Velocity correction function

The Fourier series of the triangular wave v(t) on the time axis

$$v(t) \;=\; -v_{max}\frac{4}{\pi^2}\left(cos\,\omega t + \frac{cos\,3\omega t}{3^2} + \frac{cos\,5\omega t}{5^2} + ...\right) \qquad (38)$$

is to some accuracy reproduced by the signal of the function generator driving the transducer. The deviations from the triangular wave form may be caused by deviations δa_i from the amplitudes $1/(2i+1)^2$ at

frequencies $\omega_i = (2i+1)\omega$ of the components of the series. In that case the function

$$dv(k) \;=\; \sum_i \delta a_i \, cos\,(\omega_i k) \tag{39}$$

should be a good choice for correcting the velocity scale. The continuous variable t is replaced by the channel number k corresponding to time steps Δt such that

$$\begin{aligned} v(k) + dv(k) \;&=\; -v_{max}\frac{4}{\pi^2}\left(cos\,\Omega * k + \frac{cos\,3\Omega k}{3^2} + \frac{cos\,5\Omega k}{5^2} + ...\right) \\ \Omega \;&=\; \frac{\pi}{2} \,/\, channel(v=0) \end{aligned} \tag{40}$$

is supposed to be the correct velocity to channel conversion.
However, more successfully turned out taking all frequencies $\Omega_i = i\Omega$ (i=1,2,...). The cos functions implies a symmetry which is broken by adding sin functions such that

$$dv(k) \;=\; \sum_i \delta a_i \, cos\,(\Omega_i k) + \delta b_i \, sin\,(\Omega_i k) \tag{41}$$

These two correction equations 39 and 41 allow for 4 cases using the different frequency sets $\Omega_i = i\Omega$ and $\Omega_i = (2i+1)\Omega$. Two further cases are introduced by changing the sign of the amplitudes δb_i for channels k of the second half of the spectrum. Up to 18 parameters can be declared. The summation index runs from 1-9 in case of two amplitudes $\delta a_i, \delta b_i$. The sinusoidal mode is also not free from nonlinearities of the velocity scale and can be corrected by the same functions. The amplitudes δa_i,δb_i turn out to be very small.

4.1.2 Interpolation of the theory function

The velocity scale of the theory is different from the velocity scale attached to the channels. The velocity steps $\Delta v_t = v_{tj+1} - v_{tj}$ of the theory are choosen to be larger than $4 * v_{max}/N$, with the number of channels N of the full period. Such a choice saves computation time since the number of theory points $N_t = 2 * v_{max}/\Delta v_t$ is the number of time consuming convolution integrals. The selection of the 4 equidistant theory points $v_{tj-1}, ..., v_{tj+2}$ is displayed in Fig.18. The velocity v_{i+3} attached to channel i+3 is as close as possible to v_{tj} or v_{tj+1}, the two velocities with the exact theory values th_j and th_{j+1}. The first and last sampling points are only approximated by the 3 constants of a parabola.

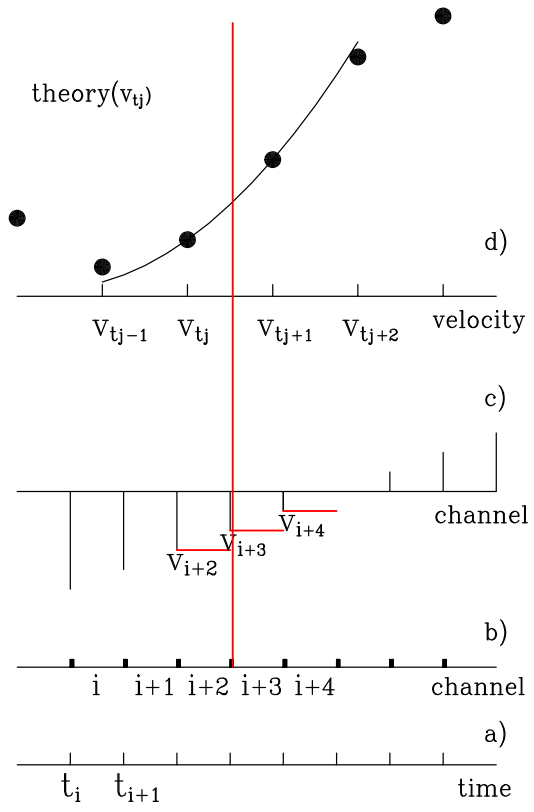

Figure 18: a) the time t with time markers t_i at the begin of channel i in b). The dwell time of the channels $t_{i+1} - t_i$ is reduced by the dead time for the channel switch from i to i+1 (indicated by the thick bars). c) The velocities at the beginning of the channels are represented by bars pointing downwards ($v < 0$), crossing v=0 and upwards ($v > 0$). A stepwise velocity increase is depicted by the horizontal red lines. The theoretical spectrum is shown in d). It has its own velocity scale v_{tj}. At v_{i+3} the function value is interpolated by a parabola calculated from v_{tj-1} until v_{tj+2}. The scale of c) is adjusted to the best fit of the interpolated values with the experimental spectrum.

The parabola $th = av^2 + bv + c$ is fitted to the theory curve at the four equidistant v-values replaced by Δv_t units ($(v - v_j)/\Delta v_t = -1, 0, 1, 2$) so that the linear equation system reads:

$$\begin{aligned} th_{j-1} &= a - b + c \\ th_j &= c \\ th_{j+1} &= a + b + c \\ th_{j+2} &= 4a + 2b + c \end{aligned} \tag{42}$$

The constants b and c can be expressed by a. $f(a)$ is minimized so that the parabola hits the two inner points (j) and (j+1) and approximates the outer points (j-1) and (j+2). The following set of equations determine

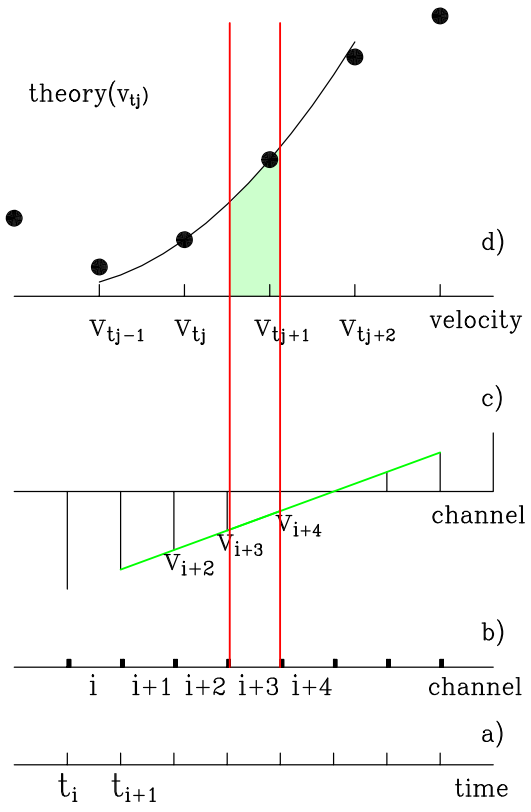

Figure 19: For a) and b) see Fig.18. c) The velocity changes linearily from v_{i+3} to v_{i+4} by a constant acceleration. d) The theoretical spectrum is integrated from the interpolated values at v_{i+3} to v_{i+4}.

a,b and c.

$$
\begin{aligned}
b &= th_{j+1} - th_j - a \qquad (43)\\
c &= th_j \\
f(a) &= (th_{j-1} - (a - b + c))^2 + (th_{j+2} - (4a + 2b + c))^2 \\
\frac{\partial f}{\partial a} &= 0 \\
=> \; a &= \frac{1}{4}(th_{j-1} + th_{j+2} - th_j - th_{j+1})
\end{aligned}
$$

Following Oshtrakha and Semionkin [32] the velocity is constant for the dwell time of a channel and is accelerated in a very short time preferably during the dead time for switching to the next channel (see Fig. 18). If this is the case, the theoretical value assigned to channel i+3 is the intersection of the red straight line with the theory curve. In Fig. 19 the velocity is linearly increasing from v_{i+3} to v_{i+4} during the time t_{i+3} till $t_{i+4} = t_{i+3} + \Delta t$. The integral from t_{i+3} till $t_{i+3} + \Delta t$ under the theoretical

curve divided by Δt corresponds to the counts collected in channel i+3.

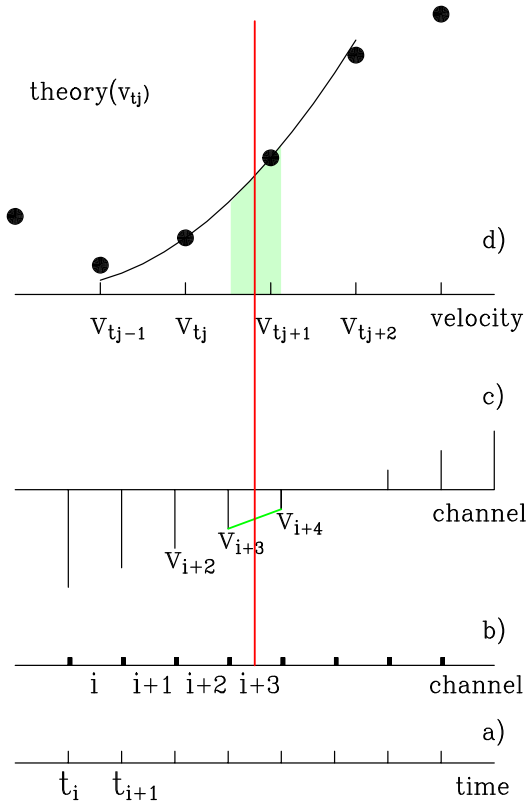

Figure 20: For a) and b) see Fig.18. c) The velocity change linearly. d) The theoretical spectrum is interpolated at $(v_{i+3} + v_{i+4})/2$.

$$
\begin{aligned}
I_{th} &= \frac{1}{\Delta t}\int_{t_{i+3}}^{t_{i+4}} th(v(t))dt \qquad (44)\\
I_{th} &= \frac{1}{\Delta t}\int_{t_{i+3}}^{t_{i+4}} th(v(t))\frac{dt}{dv}dv
\end{aligned}
$$

With the constant acceleration dv/dt and $dv/dt \cdot \Delta t = \Delta v = v_{i+4} - v_{i+3}$ the integral

$$
\begin{aligned}
I_{th} &= \frac{1}{\Delta v}\int_{t_{i+3}}^{t_{i+4}} th(v)dv \qquad (45)\\
&= \frac{1}{\Delta v}\left[\frac{1}{3}av^3 + \frac{1}{2}bv^2 + cv\right]_{t_{i+3}}^{t_{i+4}}\\
&= \frac{1}{3}a(v_{i+3}^2 + v_{i+4}^2 + v_{i+3}\cdot v_{i+4}) + \frac{1}{2}b(v_{i+3} + v_{i+4}) + c
\end{aligned}
$$

is the theoretical value of channel i+3. A linear interpolation is sufficient for small velocity steps achieved by large channel numbers. Omitting the constant a (a=0) the integral is given by

$$\begin{aligned} I_{th} &= \frac{1}{2}b(v_{i+3}+v_{i+4})+c \\ &= \frac{1}{2}(v_{i+3}+v_{i+4})(th_{j+1}-th_j)+th_j \end{aligned} \tag{46}$$

Only two values of the theory have to be calculated. The integral can also be well approximated by the theory value at the center of channel i+3 at $\frac{1}{2}(v_{i+3}+v_{i+4})$ multiplied by $\Delta v = v_{i+4}-v_{i+3}$ as is obvious from Fig. 20. The disadvantage is the recalculation of the theory at the center of the channels scaled by velocity and not by the time. The majority of the Mössbauer programs have only this possibility. It shall be noted that the intuitive choice of the center of the channel implicates a constant acceleration. The stepwise increase of the velocity as shown in Fig. 18 seems to be not realized in any of the programs.

Non-equidistant velocity axis

Eq.42 has been set up for 4 equidistant v-values $(v-v_i)/\Delta v = -1, 0, 1, 2$ with v_2 shifted to the second value. For non-equidistant v-values the 4 points reads:

$$x_i = v_i - v_2 \quad \rightarrow \quad x_1,\, x_2 = 0,\, x_3,\, x_4$$

The parabola function $th = ax^2+bx+c$ matches point number 2 and 3

$$\begin{aligned} th_2 &= c \\ th_3 &= ax_3^2+bx_3+c \end{aligned} \tag{47}$$

The th-distances at point x_1 and x_4 are minimized by

$$D = (th_1-(ax_1^2+bx_1+c))^2+(th_4-(ax_4^2+bx_+c))^2 \tag{48}$$

$$\begin{aligned} \frac{\partial D}{\partial a} &= 2(th_1-(ax_1^2+bx_1+c))(-x_1^2+\frac{\partial b}{\partial a}x_1)+ \\ &\quad 2(th_4-(ax_4^2+bx_4+c))(-x_4^2+\frac{\partial b}{\partial a}x_4) \end{aligned}$$

With $b(a) = (th_3-ax_3^2-c)/x_3$ the condition $\partial D/\partial a = 0$ gives

$$\begin{aligned} \alpha &= (th_1-c)(x_1-x_3)x_1+(th_4-c)(x_4-x_3)x_4 \\ \beta &= (th_3-c)((x_1-x_3)x_1^2+(x_4-x_3)x_4^2) \\ a &= \frac{\alpha-\beta/x_3}{(x_1-x_3)^2x_1^2+(x_4-x_3)^2x_4^2} \end{aligned} \tag{49}$$

Inserting the special case of equidistant x-values : $x_1 = -\Delta v, x_2 = 0, x_3 = \Delta v, x_4 = 2\Delta v$

$$\begin{aligned} \alpha &= (th_1 - c)2(\Delta v)^2 + (th_4 - c)2(\Delta v)^2 \\ \beta &= (th_3 - c)(-2+4)(\Delta v)^2 \\ a &= \frac{\alpha - \beta}{(4+4)(\Delta v)^4} = \frac{th_1 + th_4 - th_3 - th_2}{4(\Delta v)^2} \end{aligned}$$

4.2 Example of an α-iron spectrum

The calibration of the velocity to channel scale in principle is determined by two parameters, the maximum velocity $v_{max}[mm/s]$ or $\alpha[mm/s/channel]$ and the channel of zero velocity k_{v0} or the folding point $k_{v0}+N/4$. These two values are obtained by a fit of the positions of 6 independend lines of the $\alpha - iron$ spectrum of one of the half-period spectra.

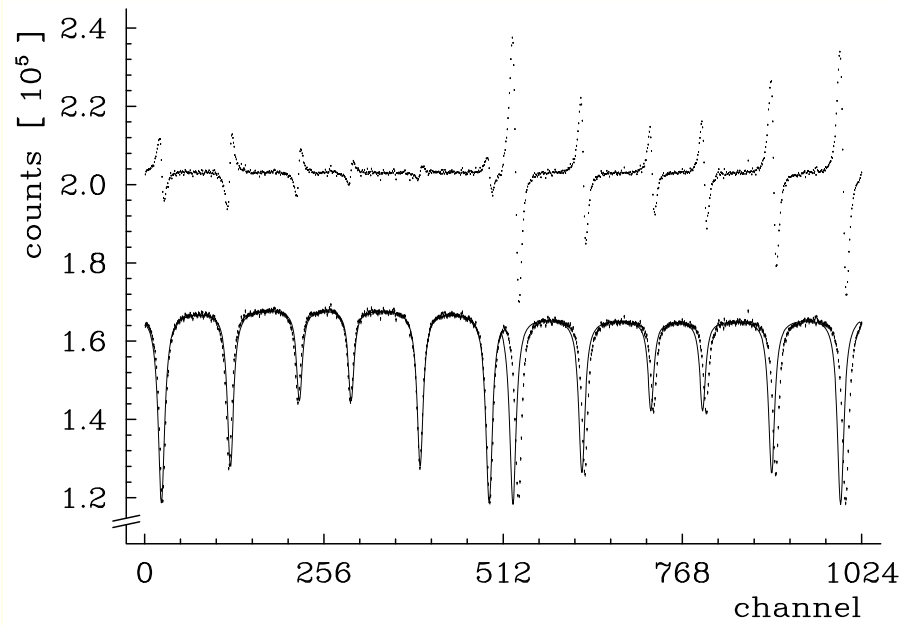

Figure 21: Calibration spectrum with $v_{max} \approx 6mm/s$ for quadrupole split Fe^{2+}-spectra. The α-iron foil of a thickness of 10μ was mounted at 45^o such that the thickness becomes $\sqrt{2} \cdot 10\mu$.

The separation of $\Delta_{1,6} = 10.64256mm/s$ devided by the difference $ch_{1,6}$ between channels of lines 1 and 6 gives $\alpha[mm/s/channel]$ and times N/4 the maximum velocity $v_{max}[mm/s]$. The zero velocity channel is obtained from the isomer shift is (referred to the source).

$$k_{v0} = \frac{1}{2}(ch_1 + ch_6) + is \cdot \alpha$$

If nonlinearity corrections dv_i are not necessary the full period spectrum should fit with the line positions.

$$\begin{aligned} p_1 &= -5.32128 + is, \quad p_2 = -3.08079 + is, \quad p_3 = -0.84029 + is \\ p_6 &= \quad 5.32128 + is, \quad p_5 = \quad 3.08079 + is, \quad p_4 = \quad 0.84029 + is \end{aligned}$$

Typically the velocity scale is nonlinear indicated by large χ^2-value imposing the positions of Eq. 50 by the Hamiltonian with an internal field of 33.05 Tesla and an isomer shift (here ^{57}Co/Rh-source) of -0.114mm/s. In Fig. 21 the left half is fitted . The nonlinearity is obvious by the large misfit of the first and second line. The fitted parameters are $v_{max} = 5.831$

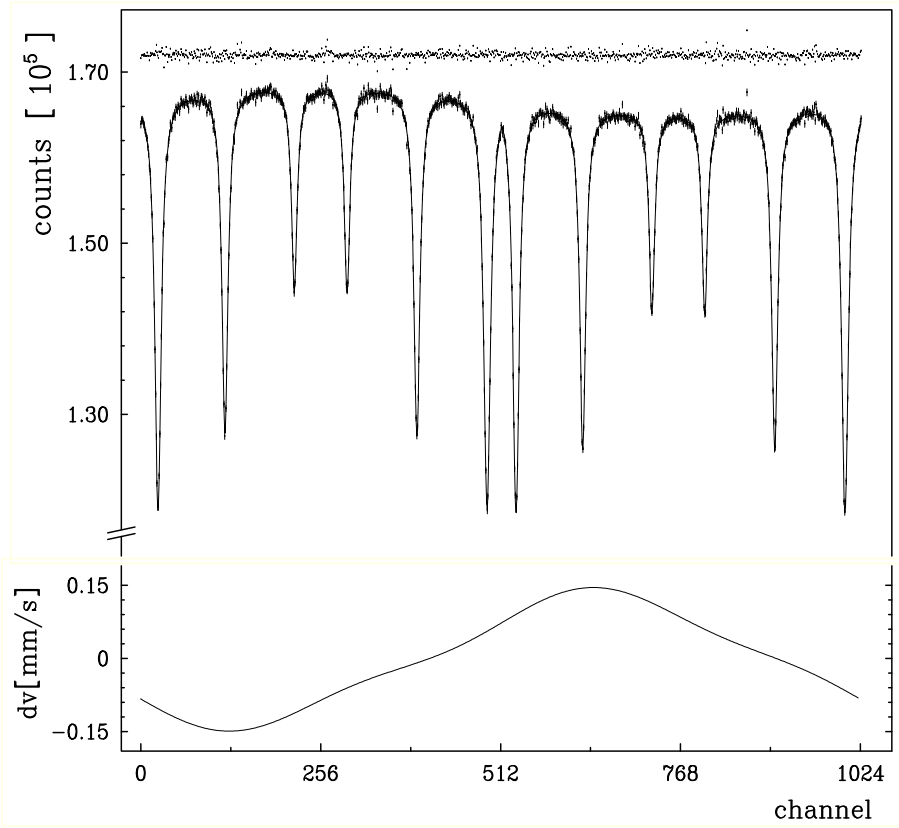

Figure 22: Calibration spectrum fitted with 6 nonlinearity parameter ($chi^2 = 1.040$). The correction of the velocity dv at each channel from equidistant values $4v_{max}/1024$ varies from -0.15mm/s to +0.15mm/s which is almost the line withs of $2\Gamma_n$ of the absorption lines.

and $k_{v0} = 253.50$ with $\chi^2 = 33$. The fit with 6 nonlinearity parameter gives a $\chi^2 = 1.026$ and a slightly larger $v_{max} = 5.864$. The folding point $k_{v0} + N/4 = 512.08$ shifts to a value almost N/2 and is also very close to the folding point 512.50 obtained by the standard procedure described in [23].

The misfit of the right half of the spectrum is much larger. The theory appears to be shifted to the left. Including the second half of the full period spectrum shown in Fig. 22 reaches $\chi^2 = 1.040$ and changes again the maximum velocity to $v_{max} = 5.918$ and the folding point by 2 channels to $k_{v0} + N/4 = 514.60$.

The fit is obtained without any line broadening of the transitions in the α-iron foil. The intensity ratio of lines (2,5)/(3,4)=2 for random oriented internal fields changes to 2.128 and the thickness of the foil comes out to be $10.62\mu m$ which is somewhat lager than the nominal value of $10\mu m$. The 5mCi-source has a slightly reduced Lamb-Mössbauer factor $f_{source} = 0.73$ instead of 0.75 (from the data sheet) and a Voigt-profile with $\sigma_{Gauss} = 0.47\Gamma_N$ and $\Gamma = 1.05 \cdot \Gamma_N$. Fitting the Voigt profile with a Lorentzian shape the width $\Gamma = 0.119mm/s$ is without doubt too large to be caused by selfabsorption effects of an old 5m Ci-source. The equipment of this measurement was not of high quality as obvious by the large nonlinearity correction so that apparative broadening independent on the velocity may be compensated by a small extra broadening of the source width.

fraction

5 Literature

References

[1] Richard J. Mathar, Solid Angle of a Rectangular Plate, http://www.mpia.de/m̃athar/public/mathar20051002.pdf, 2014.

[2] JOHN A. WEIL, TOMAS BUCH and JAMES E. CLAPP, Crystal Point Group Symmetry and Microscopic Tensor Properties in Magnetic Resonance Spectroscopy, volume 6 of *Advances in Magnetic and Optical Resonance*, p. 183 – 257. Academic Press, 1973.

[3] H. Spiering and H. Vogel, Hyperfine Interactions **3**, 221–229 (1977).

[4] James N. Bull, T. Ward. Robinson and W. Craighead Tennant, Hyperfine Interactions **94**, 347–366 (2009).

[5] James N. Bull, Christopher M. Fitchett and W. Craighead Tennant, Hyperfine Interactions **198**, 273–293 (2010).

[6] James N. Bull, Robert G. A. R. Maclagan and a W. Craighead Tennant, J. Phys. Chem. A **115**, 10655–10663 (2011).

[7] Mahmoud I. Abbas, Sami Hammoud, Tarek Ibrahim and Mohamed Sakr, Nuclear Instruments and Methods in Physics Research Section A: Accelerators, Spectrometers, Detectors and Associated Equipment **771**, 121 – 125 (2015).

[8] Mahmoud I. Abbas, Sami Hammoud, Tarek Ibrahim and Mohamed Sakr, Nuclear Instruments and Methods in Physics Research Section A: Accelerators, Spectrometers, Detectors and Associated Equipment **771**, 121 – 125 (2015).

[9] Glenn E Knoll, *Radiation Detection and Measurement*, (https://phyusdb.files.wordpress.com/2013/03/ radiationdetectionandmeasurementbyknoll.pdf, John Wiley & Sons, Inc., 1999).

[10] Jörg W. Müller, Nuclear Instruments and Methods **117**, 401 – 404 (1974).

[11] Malvin C. Teich, Biol. Cybern. **53**, 121–124 (1985).

[12] R. E. Odeh and J. O. Evans, Applied Statistics **23**, 96–97 (1974).

[13] R. Riesenman, J. Steger and E. Kostiner, Nuclear Instruments and Methods **72**, 109 – 110 (1969).

[14] D. Crespo and J. Parellada, Hyperfine Interactions **29**, 1539–1542 (1986).

[15] H. Flores-Llamas and R. Zamorano-Ulloa, Nuclear Instruments and Methods in Physics Research Section B: Beam Interactions with Materials and Atoms **58**, 272 – 277 (1991).

[16] J. N. Bull, W. C. Tennant, T. Boffa Ballaran, F. Nestola and C. A. McCammon, Physics and Chemistry of Minerals **39**, 561–575 (2012).

[17] M. Blume and O.C. Kistner, Phys. Rev. **171**, 417 (1968).

[18] Patrick McQuighan, SIMULATING THE POISSON PROCESS, http://www.math.uchicago.edu/ may/VIGRE/VIGRE2010/ REUPapers/Mcquighan.pdf, 2010.

[19] Art B. Owen, Monte Carlo theory, methods and examples, http://statweb.stanford.edu/ owen/mc/Ch-nonunifrng.pdf, 2013, chapter 4:Non-uniform Random Numbers.

[20] Jari Hjollum and Morten Bo Madsen, **Fit;o)** - A Mössbauer spectrum fitting program, Earth and Planetary Physics, Juliane Maries vej 30, Niels Bohr Institute, University of Copenhagen, Denmark, 2009.

[21] Thomas A. Kent and Ion Prisecaru, Program **WMOSS4**, url = http://www.wmoss.org, 2013.

[22] R. N. Brand, Program **NORMOS**, url = http://www.wissel-gmbh.de, 2006.

[23] Z. Klencsár, Program **MOSSWINN**, url = http://www.mosswinn .com, 2014.

[24] Szilárd Sajti, Program **FitSuite**, url = http://www.fs.kfki.hu, 2009.

[25] Sirko Kamusell, Program **Moessfit**, url = http://www.tu-dresden.de/die tu dresden/fakultaeten/ fakultaet mathematik und naturwissenschaften/ fachrichtung physik/ifp/mitarbeiter ifp/mitarbeiter details/Moessfit, 2014.

[26] Tomáš Žák, Program **CONFIT2000** Mössbauer spectra fitting, url=http://www.ipm.cz/group/emp/confita.html, 2017.

[27] Lukasz Duraj and Krzysztof Ruebenbauer, Program **Mosgraf**-2009: The Mössbauer data processing suite of applications, NUKLEONIKA 58,16-16 (2013), 2013.

[28] Ken Lagarec and Denis G Rancourt, Program **Recoil**-Mössbauer Spectral Analysis Software for Windows, url =http://www.academia.edu/1072429/Recoil-Mössbauer_Spectral_Analysis_Software_for_Windows, 1999.

[29] Kristjan Jonsson, Program **Mfit** : A Program For Fitting Mössbauer Spectra, url=https://notendur.hi.is/kj/mfit, 1999.

[30] info@wissel.eu, WissEl - Wissenschaftliche Elektronik GmbH, url=http://www.wissel-instruments.de, 2017.

[31] info@fastcomtec.com, FAST ComTec Communication Technology GmbH, url=https://www.fastcomtec.com/, 2017.

[32] Michael I. Oshtrakha and Vladimir A. Semionkin, AIP Conf. Proc. **doi: 10.1063/1.4966015**, 020019–1 – 020019–16 (2016).